RESEARCH ARTICLE | NOVEMBER 07 2025

Effect of coupled surge-pitch motions on the wake characteristics of floating offshore wind turbines under atmospheric boundary layer inflows ⊘

Mingqiu Liu (刘明秋) ⑩ ; Yao Zhong (钟耀); Weiwen Zhao (赵伟文) ➡ ⑩ ; Decheng Wan (万德成) ⑩



Physics of Fluids 37, 115115 (2025) https://doi.org/10.1063/5.0293258









# Effect of coupled surge-pitch motions on the wake characteristics of floating offshore wind turbines under atmospheric boundary layer inflows

Cite as: Phys. Fluids 37, 115115 (2025); doi: 10.1063/5.0293258 Submitted: 26 July 2025 · Accepted: 20 October 2025 · Published Online: 7 November 2025











Mingqiu Liu (刘明秋), 1 fo Yao Zhong (钟耀), 2 Weiwen Zhao (赵伟文), 1 a) fo and Decheng Wan (万德成) fo





**AFFILIATIONS** 

Computational Marine Hydrodynamics Lab (CMHL), School of Ocean and Civil Engineering, Shanghai Jiao Tong University, Shanghai, China

<sup>2</sup>Zhongnan Engineering Corporation Limited, Changsha, China

## **ABSTRACT**

This study presents a numerical investigation of floating offshore wind turbines (FOWTs) subjected to coupled surge-pitch motions under atmospheric boundary layer (ABL) inflows. Large eddy simulation combined with the actuator line model is used to simulate FOWTs, with a focus on analyzing aerodynamic performance and wake characteristics. Results indicate that platform motion has a limited impact on timeaveraged power and thrust but causes pronounced fluctuations in instantaneous power and thrust. Compared to fixed-bottom wind turbines, FOWTs exhibit faster wake recovery under ABL conditions, particularly within 6D (D represents the rotor diameter) downstream. Gaussian fitting shows that FOWTs with larger platform motion amplitudes and higher frequencies exhibit smaller standard deviations and larger centerline displacements. Phase-averaged vorticity analysis reveals that platform motion induces periodic vortex structures near the shear layer, which remain coherent within the first 4D downstream. Dynamic mode decomposition analysis is performed to examine the unsteady evolution of FOWT wakes. The results show that the dominant modes are primarily influenced by inflow turbulence, while platform motion excites response modes with periodic spatial structures. Although the energy contribution of these motion-induced modes is generally limited, low-frequency motions tend to induce higher-energy modes and more pronounced wake responses. These findings provide valuable insight for analytical wake models, reduced-order modeling, and future studies on complex platform motions and multi-turbine interactions.

Published under an exclusive license by AIP Publishing. https://doi.org/10.1063/5.0293258

## I. INTRODUCTION

In recent years, offshore wind energy has experienced rapid development worldwide, owing to its numerous advantages, including independence from land-use constraints, abundant wind resources, and proximity to economic zones. The development of offshore wind energy is gradually moving into deep-sea areas, where floating offshore wind turbines (FOWTs) become more technically viable with greater water depth. When subjected to combined wind, wave, and current loads, the FOWT platform undergoes six degrees of freedom (6-DOF) motion, which significantly affects the wake characteristics of the turbine. Wake characteristics are a critical factor influencing the operational efficiency of wind farms, as they directly impact the fatigue loads and power output of downstream wind turbines.<sup>2</sup> Therefore, investigating the effects of platform motion on the FOWT wake characteristics is essential for optimizing the layout of floating wind farms and improving their overall performance.

Various numerical methods have been employed to investigate the aerodynamic performance and wake characteristics of FOWTs. Free vortex methods based on potential flow theory<sup>3–5</sup> offer high computational efficiency and can reasonably predict the rotor thrust and power of FOWTs. However, these methods are limited in accurately capturing detailed wake structures. In contrast, computational fluid dynamics (CFD) methods provide high-fidelity predictions of both aerodynamic performance and the detailed flow field. Consequently, with the advances of computational resources, CFD approaches, particularly large eddy simulation (LES) and Reynolds-averaged Navier-Stokes (RANS) methods, have been increasingly adopted for studying FOWT aerodynamics and wake characteristics. Within CFD-based approaches, modeling strategies for FOWTs can be categorized into geometry-resolved methods and actuator-based methods. The geometry-resolved method involves explicitly meshing the wind turbine geometry and surrounding flow field within the computational

a)Author to whom correspondence should be addressed: weiwen.zhao@sjtu.edu.cn

domain. It typically incorporates sliding mesh or overset mesh methods to simulate wind turbine motion, enabling direct modeling of the interaction between the wind turbine and the flow field. Tran and Kim<sup>6</sup> found that surge motion significantly affects the aerodynamic performance of FOWTs, depending on both the amplitude and frequency of the motion. Fang et al. 7,8 employed improved delayed detached eddy simulation (IDDES) to simulate FOWTs under pitch and surge motions. Their results showed that surge motion influences wake recovery, while pitch motion markedly alters aerodynamic performance, with strong dependence on its amplitude and period. Chen et al.9 investigated the effects of individual and combined surge and pitch motions on aerodynamic performance, finding that combined motion led to a 6.32% reduction in average power output compared to pitch motion alone and increased fluctuations in blade loads. Chen et al.10 reported that surge motion accelerates wake recovery, with faster recovery rates observed at larger amplitudes. Moreover, highfrequency surge motions predominantly influence the near-wake region, while frequency changing has limited impact on the far-wake. Guo et al. 11 and Cai et al. 12 analyzed the aerodynamic effects of combined surge and pitch motions with different phase differences, demonstrating that in-phase motion induces the largest fluctuations in thrust and power, whereas anti-phase motion significantly mitigates such fluctuations. Wang et al. 13 found that pitch motions with lower frequency and amplitude result in greater wake energy losses. However, due to the substantial mesh requirements near the wind turbine, the geometry-resolved methods are mainly used to study the aerodynamic performance or near-wake characteristics of a single wind turbine due to computational limitations.

In contrast, actuator-based methods, such as the actuator line model (ALM), apply the aerodynamic forces exerted by the wind turbine on the flow field in the form of body forces. These methods eliminate the need for meshing detailed wind turbine geometries, thus significantly reducing the computational cost. As a result, actuatorbased methods have been widely used in the study of FOWT wake characteristics. Li et al. 14 investigated the mechanism of wake meandering induced by sway and roll motions, analyzing the effects of varying amplitudes, frequencies, and inflow conditions on wake instability. Under low-turbulence inflow, significant wake meandering occurs when the motion Strouhal number ranges from 0.2 to 0.6. In contrast, under high-turbulence inflow, wake meandering is primarily driven by ambient turbulence. Arabgolarcheh et al. 15,16 simulated two FOWTs arranged in tandem and studied the effects of surge phase differences and upstream wind turbine pitch amplitudes on the performance and wake characteristics of the downstream wind turbine. The results indicated that increasing the pitch amplitude enhanced power output for both wind turbines. However, out-of-phase motions significantly increased fatigue loads, with the blade root bending moments increasing by up to 100%. Yang<sup>17</sup> employed an improved actuator curve embedding method to simulate the aerodynamic performance and wake evolution of an FOWT under surge motion. Their study revealed that the spacing between vortex rings in the wake is mainly determined by the surge period, with minimal influence from amplitude. Li et al. 18 examined the effects of different inflow turbulence intensities and surge amplitudes and periods on the aerodynamic performance and wake characteristics of an FOWT. Through phaseaveraging techniques, they identified periodic coherent structures induced by surge motion in the vorticity field, which enhanced

downstream momentum transport and accelerated wake recovery. Yang et al. 19 used a modified actuator disk model to simulate FOWTs under various sway amplitudes and proposed a new analytical wake model based on the simulation results. Zhou et al.<sup>20</sup> investigated the impact of 6-DOF motion on FOWT aerodynamic performance and wake behavior. They found that translational motions reduced wake length to approximately 60%-70% of that of fixed-bottom wind turbines (FBWTs), whereas rotational motions increased wake length to about 110%-120%. In addition, some researchers<sup>21-23</sup> have integrated ALM with hydrodynamic and mooring modules to conduct fully coupled simulations of FOWTs, enabling the analysis of platform motion response, mooring tension, and aerodynamic performance. Current research has established some fundamental understanding of FOWT wake characteristics, for instance, FOWTs tend to exhibit faster wake recovery compared to FBWTs. However, most existing studies have been conducted under laminar inflow conditions, with relatively limited investigations under turbulent inflow, particularly atmospheric turbulence, which does not accurately reflect real-world operating environments. Furthermore, studies of combined motions are still scarce, and the mechanisms governing wake evolution under motioninduced influences remain to be thoroughly studied.

Dynamic mode decomposition (DMD), as a data-driven method, has proven to be an effective tool for investigating the evolution mechanisms of wind turbine wakes. DMD can extract dominant wake modes, characterize their frequency content, and capture their temporal evolution. In recent years, an increasing number of studies have applied DMD to analyze wind turbine wake dynamics. De Cillis et al.<sup>24</sup> employed sparsity-promoting DMD to investigate the influence of inflow turbulence on wake modes. Their findings showed that under turbulent inflow conditions, high-frequency modes were replaced by lower-frequency modes within the range of wake meandering frequencies, highlighting the importance of considering atmospheric turbulence effects in wake modeling. Wang et al.<sup>25</sup> studied the evolution of wake structures behind FOWTs under various surge amplitudes and frequencies. Their results revealed that increasing the motion frequency reduced the spatial extent of wake velocity fluctuations, while increasing the amplitude intensified the magnitude of velocity deficit oscillations. Manganelli et al.26 investigated the impact of wind veer induced by the Coriolis force on the coherent structures within the wind turbine wake. They found that the veer-induced structures exhibited spanwise velocity components of the same order of magnitude as the streamwise component and had an oblique spatial shape. Zhang et al. 27 conducted simulations of wind turbines at both model and full scales. Their analysis revealed consistent vortex generation, entrainment, and breakdown processes across scales. However, the modelscale cases exhibited lower turbulence intensity and slower wake recovery. Overall, DMD enables the identification of various frequency components and their dynamic behaviors within the wind turbine wake, offering deeper insight into wake physics.

Under atmospheric boundary layer (ABL) inflow conditions, the differences in wake characteristics between FOWTs and FBWTs under combined motion are not yet well understood, and the underlying wake evolution mechanisms require further investigation. Therefore, this study investigates the influence of surge–pitch coupled motion on the wake characteristics of an FOWT under ABL inflow. The ABL inflow is generated using the precursor simulation approach, and LES is adopted as the turbulence modeling method. The FOWT is modeled

using the ALM to balance computational cost and wake simulation accuracy. A series of cases are simulated, involving different ambient turbulence intensities and combinations of motion amplitudes and periods. The three-dimensional wake structures of the FOWT are analyzed, and the DMD method is employed to investigate the wake evolution mechanisms under coupled motion. Compared with existing studies that typically considered laminar or non-ABL inflows, 9,11,12,2 addressed individual platform motions, 8,13,25 or provided limited use of modal decomposition techniques, the present work highlights three main contributions: (i) investigating the wake evolution of an FOWT under realistic ABL inflow conditions; (ii) examining the wake characteristics of an FOWT subjected to coupled surge-pitch motions; and (iii) applying the DMD approach to identify dominant unsteady modes and elucidate their contribution to wake dynamics under coupled motion. These contributions provide a deeper understanding of the wake evolution mechanisms of FOWTs and support the development of parameterized analytical wake models.

The structure of this paper is as follows. Section II presents the numerical methods, including the governing equations, the turbulence model, and the ALM used for modeling the FOWT. Section III describes the simulation setup, mesh independence verification, and solver validation. Section IV provides an analysis of the numerical simulation results, including quantitative evaluations of the FOWT wake structure under different conditions, comparative analysis of velocity deficit and turbulence intensity increase in the wake region, and the extraction of coherent structures and their evolution using DMD, with a particular focus on identifying core structures and analyzing their dynamic characteristics within the wake. Finally, Sec. V summarizes the work and presents the main conclusions.

## II. NUMERICAL METHODS

## A. Large eddy simulation

LES is a method that lies between direct numerical simulation (DNS) and Reynolds-averaged Navier-Stokes (RANS) approaches. It is suitable for capturing unsteady flow behavior and has been widely used in the simulation of wind turbine wakes. The fundamental concept of LES is to separate large and small turbulent eddies through a spatial filtering operation. The large-scale eddies are resolved directly, while the small-scale eddies are modeled using a subgrid-scale model. In the simulation, the filter size is defined as the cubic root of the cell volume. The filtered incompressible continuity and momentum equations are expressed, incorporating the effects of Coriolis force, buoyancy, and forces exerted by the wind turbine, as follows:

$$\frac{\partial \bar{u}_i}{\partial r_i} = 0,$$
 (1)

$$\frac{\partial \bar{u}_{i}}{\partial x_{i}} = 0, \tag{1}$$

$$\frac{\partial \bar{u}_{i}}{\partial t} + \frac{\partial (\bar{u}_{i}\bar{u}_{j})}{\partial x_{j}} = -\frac{\partial \hat{p}}{\partial x_{i}} - \frac{\partial \tau_{ij}^{D}}{\partial x_{j}} - \frac{1}{\rho_{0}} \frac{\partial p_{0}(x, y)}{\partial x_{i}} + \frac{1}{\rho_{0}} F_{i} - \varepsilon_{ijk}^{f} \bar{u}_{k}, \tag{2}$$

where the overbar indicates the spatially resolved quantities; t represents time; u denotes the wind velocity;  $\rho_0$  is the reference air density;  $\tau_{ii}^D$  is the deviatoric component of the wind stress tenor;  $F_i$  represents the force exerted by the wind turbine; g denotes the gravitational acceleration;  $\varepsilon_{ijk}$  is the alternating unit tensor; f represents the Coriolis parameter; and  $\hat{p}$  denotes the modified pressure, defined by  $\hat{p} = (\bar{p} - p_0 + \rho gz)/\rho_0 + \tau_{kk}/3$ , where  $\bar{p}$  represents the filtered pressure and  $p_0$  denotes the static pressure.

The stress  $\tau_{ii}^D$  is computed based on the Smagorinsky subgridscale model,<sup>28</sup> and its formulation is given as follows:

$$\tau_{ii}^D = -2(c_s \Delta)^2 |\bar{S}| \bar{S}_{ii}, \tag{3}$$

where  $c_s$  denotes the Smagorinsky constant, set at 0.13;  $\Delta$  denotes the filter size;  $\bar{S}_{ij} = (\partial \bar{u}_i/\partial x_j + \partial \bar{u}_j/\partial x_i)/2$  represents the resolved strain rate tensor; and  $|\bar{S}| = \sqrt{2\bar{S}_{ij}\bar{S}_{ij}}$  denotes the norm of the resolved strain rate tensor. More details on the governing equations can be found in Churchfield et al.2

#### B. Actuator line model

ALM is an actuator-based approach that simplifies wind turbine blades into lines of discrete actuator points distributed along the radial direction. Each actuator point represents a small segment of a blade element, and the aerodynamic forces at these points are computed based on blade element theory. These forces are subsequently distributed into the surrounding flow field as body forces via a smoothing kernel. This circumvents the geometric complexity of geometryresolved methods and offers a balance between accuracy and computational efficiency. The method was first proposed by Sørensen and Shen<sup>30</sup> and is widely used for simulating wind turbine wakes. The body force of the actuator point can be expressed as

$$f = (L, D) = \frac{1}{2} \rho U_{rel}^2 cdr(C_L \vec{e}_L + C_D \vec{e}_D), \tag{4}$$

where L and D are the lift and drag forces, respectively;  $U_{rel}$  is the relative wind speed; c is the chord length; dr represents the width of the blade element;  $C_L$  and  $C_d$  represent the lift and drag coefficients, respectively;  $\vec{e}_L$  and  $\vec{e}_D$  are the unit vectors of lift and drag, respectively.

Early implementations of ALM are primarily developed for simulating FBWTs. To extend the model to FOWTs, additional velocity components induced by platform motion are incorporated into the calculation of the relative wind speed. Figure 1 illustrates the velocity vectors of the blade element. Here,  $U_M$  denotes the additional velocity induced by platform motion,  $\Omega$  is the rotor speed, U represents the inflow wind speed, and the subscripts  $\theta$  and Z, respectively,

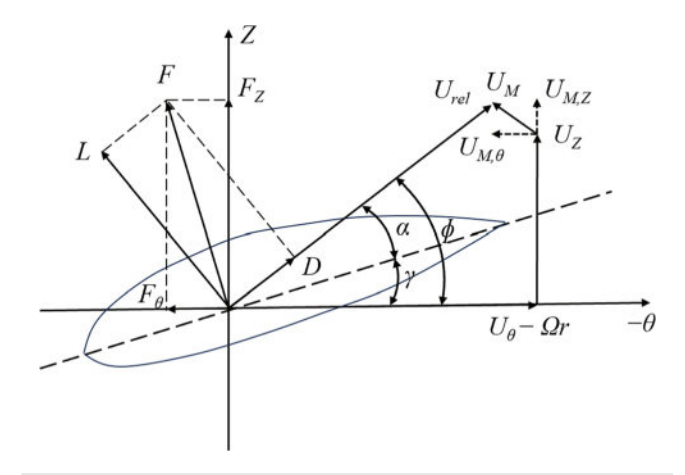


FIG. 1. Velocity vectors of the blade element

represent the tangential and axial components. The local attack angle  $\boldsymbol{\alpha}$  is defined as

$$\alpha = \varphi - \beta, \varphi = \tan^{-1} \left( \frac{U_Z + U_{M,Z}}{\Omega r + U_{M,\theta} - U_{\theta}} \right), \tag{5}$$

where  $\varphi$  is the local inflow angle,  $\beta$  denotes the local pitch angle, and r represents the radial distance between the local blade element and rotor center. As described above, when incorporating the wind turbine body force term into the governing equations, it is essential to apply a smoothing procedure to the body force distribution to avoid numerical singularities. The Gaussian kernel function is employed for this purpose, which ensures numerical stability by distributing the forces smoothly over the computational grid. Further details of the ALM can be found in Xu *et al.*<sup>23</sup>

## III. NUMERICAL SIMULATION

#### A. Numerical setup

The solver used in this study is the open-source software SOWFA (Simulator for Wind Farm Applications), developed by the National Renewable Energy Laboratory (NREL) based on OpenFOAM for wind farm simulations. SOWFA is capable of simulating FBWTs and can be coupled with FAST to enable simulations of FOWTs.<sup>29</sup> In this study, the original SOWFA framework is extended by implementing additional code to incorporate prescribed 6-DOF forced motions for FOWT simulations. Specifically, the actuator line module is modified to update actuator point positions based on the prescribed platform motions. The relative velocity of each actuator point, obtained from the combination of inflow wind speed, rotor speed, and platform motion velocity, is integrated in time to yield the relative displacement, which was then applied to update the actuator point positions. The wind turbine model used in this study is the NREL 5 MW reference turbine,<sup>31</sup> with a rotor diameter (D) of 126 m and a hub height of 90 m. The rated wind speed is 11.4 m/s, and the rated rotational speed is 12.1 rpm. To control external influencing factors and isolate the effects under investigation, control systems, aeroelastic effects, and the tower structure are excluded from the simulations in this study. These simplifications may in principle affect the predicted mean power, load fluctuations, and wake recovery. Previous studies suggest that aeroelastic effects cause only slight reductions in mean power and load fluctuations, with a minor decrease in near-wake velocity deficit, 32,33 while tower-induced effects mainly lead to small modifications in near-wake recovery with negligible influence on overall performance.<sup>34,35</sup> Such differences are not expected to alter the main conclusions of the present study. The influence of the control system is further examined in Appendix A. Unless otherwise specified, the operating conditions are set to the rated state of the wind turbine. Although these simplifications are necessary to isolate the aerodynamic influence of platform motion, it is important to recognize that these factors may affect the power and wake characteristics of FOWTs in practical applications. In practical conditions, advanced control strategies can effectively suppress platform motions and reduce power fluctuations. Meanwhile, aeroelastic effects may slightly accelerate wake recovery, whereas tower-induced effects have a limited influence on the overall power output but can slightly increase the near-wake velocity deficit due to flow separation and tower shadow.

The numerical simulation consists of two stages. The first stage is the precursor simulation and the second stage is the wind turbine simulation. In the precursor stage, the ABL inflow is generated using a precursor simulation method. The computational domain is a rectangular box measuring  $3000 \times 1000 \times 1000 \,\mathrm{m}^3$ , as shown in Fig. 2. The grid is uniformly set to 10 m in all three directions, resulting in a total of 3  $\times$  10<sup>6</sup> cells. Cyclic boundary conditions are applied on all lateral sides, a slip boundary condition is used at the top, and the Moeng wall model<sup>36</sup> is employed at the bottom to compute shear stress. The inflow wind enters along the positive x-direction, with a wind speed of 11.4 m/s at the hub height (90 m). To achieve a quasi-equilibrium ABL flow field, the precursor simulation is run for 18 000 s with a time step of 0.2 s. Additionally, an extra 1000 s of continuous simulation is performed to generate time-resolved inflow boundary conditions for the wind turbine simulation stage. In this study, three precursor simulations with varying levels of ambient turbulence intensity are conducted to investigate the influence of turbulence intensity on the wake structure of the FOWT. The streamwise turbulence intensities at hub height are 2.82%, 6.02%, and 9.02%, corresponding to power-law wind shear exponents of 0.035, 0.105, and 0.143, respectively. Among them, the case with a turbulence intensity of 6.02% is selected as the reference case. All three cases fall within the range of offshore turbulence intensity, which is approximately 2.5%-12.0%.

In the wind turbine simulation stage, the interaction between the FOWT and the ABL flow field is simulated. The computational domain and the initial mesh are identical to those used in the precursor stage. Note that the inlet boundary condition is time-varying and prescribed using a mapping approach based on flow fields obtained from the precursor simulation, while a zero-gradient pressure boundary condition is applied at the outlet. The wind turbine is initially positioned 6D downstream of the inlet, as indicated by the black short line in Fig. 3 (D represents the rotor diameter). Based on the initial mesh, two levels of mesh refinement are applied in a rectangular region surrounding the wind turbine. The first-level refinement region extends 13D, 4D, and 2.5D in the x, y, and z directions, respectively, and begins 2.5D upstream of the turbine. The second-level refinement region spans 12 D, 3 D, and 2 D in the x, y, and z directions, respectively, and starts 2D upstream of the turbine. The grid resolution within the refined region is  $2.5 \times 2.5 \times 2.5$  m<sup>3</sup>, resulting in a total of approximately  $13 \times 10^6$  cells. A time step of 0.02 s is chosen to meet the Courant-Friedrichs-Lewy (CFL) stability condition. The simulation is executed for a total duration of 1000 s with this fixed time step size. The wind turbine wake undergoes a transitional development phase

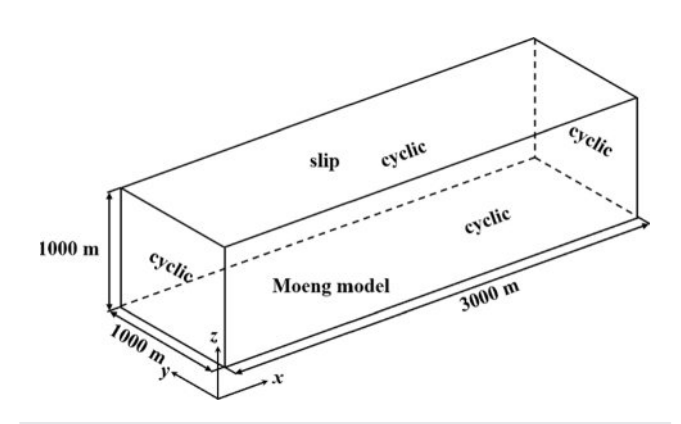
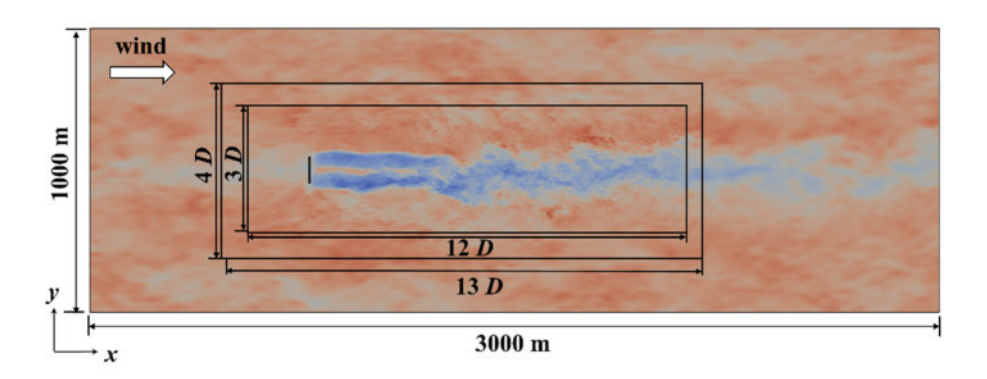


**FIG. 2.** The computational domain.



(a) xy plane

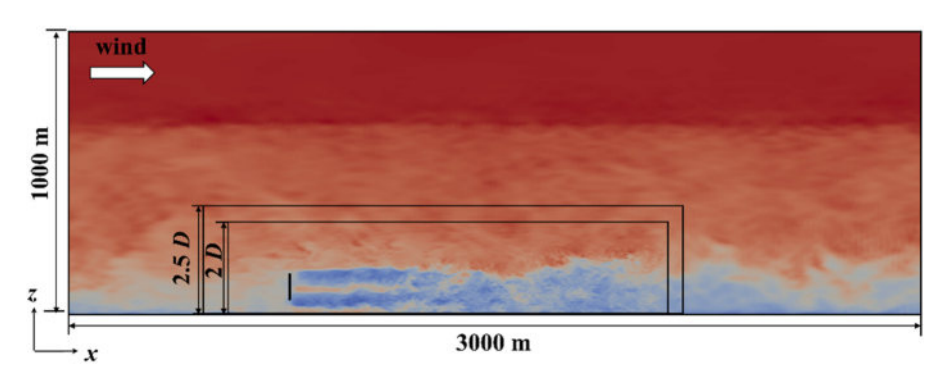


**FIG. 3.** Schematic of the computational domain and mesh refinement zone.

(b) xz plane

before reaching a statistically steady state. To ensure the analysis is based on fully developed flow conditions, the first 400 s of data are discarded, and the subsequent 600 s of stable data are used for further analysis.

In this study, both surge and pitch motions are prescribed as regular sinusoidal oscillations. The surge motion corresponds to a back-and-forth translation along the x-axis, with its displacement and velocity defined as follows:

$$X_s(t) = A_s \sin(2\pi f_s t), \tag{6}$$

$$v_s(t) = 2\pi f_s A_s \cos(2\pi f_s t), \tag{7}$$

where  $A_s$  represents the surge motion amplitude and  $f_s$  denotes the surge motion frequency. The pitch motion is defined as a fore-and-aft rotation about the y-axis, centered at a point located 90 m below the wind turbine hub. The pitch angle and angular velocity are defined as follows:

$$\theta_p(t) = A_p \sin(2\pi f_p t), \tag{8}$$

$$\omega_p(t) = 2\pi f_p A_p \cos(2\pi f_p t), \tag{9}$$

where  $A_p$  represents the pitch motion amplitude and  $f_p$  denotes the pitch motion frequency. The simulation cases are summarized in Table I. The first three cases represent FBWTs.  $I_u$  denotes the streamwise turbulence intensity and is used to distinguish the inflow conditions corresponding to the three precursor simulations described

earlier. Unless otherwise specified, all turbulence intensities mentioned hereafter refer to the streamwise turbulence intensity. Case 5, with an amplitude of 4 m and a frequency of 0.1 Hz, is selected as the reference case. The chosen frequency corresponds to typical wave frequencies observed in offshore environments.<sup>38</sup> At this frequency, the response amplitude operators (RAOs) for both surge and pitch motions are approximately two.<sup>39</sup> To ensure a controlled comparison, the ratios between the amplitudes of surge and pitch motions are kept constant across the other frequency cases. The motion amplitudes are set to

TABLE I. Cases settings.

Case	$A_s$ (m)	$f_s$ (Hz)	$A_p\left(^{\circ}\right)$	$f_p$ (Hz)	$I_u$ (%)
1					2.82
2					6.02
3					9.02
4	2	0.1	2	0.1	6.02
5	4	0.1	4	0.1	6.02
6	8	0.1	8	0.1	6.02
7	4	0.05	4	0.05	6.02
8	4	0.2	4	0.2	6.02
9	4	0.1	4	0.1	2.82
10	4	0.1	4	0.1	9.02

relatively large values in order to better investigate the influence of platform motion on wake characteristics.

### B. Mesh and time step convergence study

To verify mesh convergence, three mesh resolutions are designed and labeled as coarse, medium, and fine. The mesh resolutions in the region near the wind turbine are  $5 \times 5 \times 5$  m<sup>3</sup>,  $2.5 \times 2.5 \times 2.5$  m<sup>3</sup>, and  $1.25 \times 1.25 \times 1.25$  m<sup>3</sup>, corresponding to the coarse, medium, and fine grids, respectively. The rotor-plane resolution of the three meshes corresponds to approximately 25, 50, and 100 cells across the rotor diameter, respectively. To reduce computational cost, the mesh refinement region in the mesh convergence study is limited to within 3D downstream of the wind turbine. The total cell counts for the coarse, medium, and fine meshes are approximately  $341 \times 10^6$ ,  $715 \times 10^6$ , and 2941 × 10<sup>6</sup>, respectively. All other simulation settings are consistent with case 2. The results for the three mesh resolutions are summarized in Table II, where the percentage values indicate the deviation relative to those obtained with the fine mesh. The mesh independence study shows that the power and thrust computed using the coarse mesh are in close agreement with the fine mesh results. When the mesh resolution is refined to  $2.5 \times 2.5 \times 2.5$  m<sup>3</sup>, the differences in power and thrust become negligible. Therefore, to balance numerical accuracy and computational cost, the medium resolution mesh is adopted for the wind turbine simulations. To further assess the time step convergence, three different time steps 0.0225, 0.02, and 0.0175 s are tested. The aerodynamic power and thrust obtained from these cases are summarized in Table III. The results show that the variations in power and thrust among the three time steps are negligible, indicating that the solution is sufficiently time-converged. Based on this assessment, a time step of 0.02 s is selected for the simulations.

### C. Numerical validation

The characteristics of the ABL flow field generated by the precursor simulation are validated in this study. The validation is

TABLE II. Aerodynamic power and thrust for different mesh resolutions.

		Power (MW)			
Case Mesh resolution		Max	Min	Mean	
Coarse	$5 \times 5 \times 5 \text{ m}^3$	6.39 (4.41%)	3.70 (3.93%)	5.14 (4.47%)	
Medium	$2.5\times2.5\times2.5~\text{m}^3$	6.22 (1.63%)	3.53 (-0.84%)	4.94 (0.41%)	
Fine	$1.25 \times 1.25 \times 1.25 \text{ m}^3$		3.56	4.92	
		Thrust (kN)			
Case	Mesh resolution	Max	Min	Mean	
Coarse	$5 \times 5 \times 5 \text{ m}^3$	846 (1.44%)	674 (0.60%)	773 (1.18%)	
Medium	$2.5\times2.5\times2.5~\text{m}^3$	839 (0.60%)	667 (-0.45%)	764 (0%)	
Fine	$1.25 \times 1.25 \times 1.25 \text{ m}^3$	834	670	764	

TABLE III. Aerodynamic power and thrust for different time steps.

		Power (MW)		
Time step (s)	Max	Min	Mean	
0.0225	6.18 (-0.64%)	3.52 (-0.28%)	4.93 (-0.40%)	
0.02	6.22	3.53	4.94	
0.0175	(0%) 6.22	(0%) 3.53	(0.40%) 4.95	
		Thrust (kN)		
Time step (s)	Max	Min	Mean	
0.0225	836	668	763	
	(0.84%)	(-1.18%)	(-0.13%)	
0.02	839	668	764	
	(1.21%)	(-1.18%)	(0%)	
0.0175	829	676	764	

based on the reference case described earlier. Figure 4 presents the time-averaged vertical profiles of wind speed, wind direction, and turbulence intensity. In the figure, "Low," "Medium," and "High" correspond to the streamwise turbulence intensities at hub height of 2.82%, 6.02%, and 9.02%, respectively, representing three ABL inflow conditions. The wind speed profiles exhibit a clear shear, which follow the general trend of the power-law wind shear model and yield a hub-height wind speed of 11.4 m/s, consistent with the rated value. Additionally, the Coriolis force is considered in the simulation, resulting in a slight height-dependent deviation in wind direction (wind veer phenomenon), which is consistent with real ABL conditions. The streamwise turbulence intensity gradually decreases with height for all three inflow cases.

Figure 5 shows the time histories and corresponding power spectral densities (PSDs) of the three velocity components, sampled on the xy plane at hub height, in the reference case. As observed, all three components exhibit significant temporal fluctuations. Moreover, the spectral analysis reveals that the PSDs closely follow the -5/3 slope across a wide frequency range, indicating that the inertial subrange is well resolved. <sup>29</sup> This confirms that LES accurately captures the energy cascade in the ABL.

To assess the reliability and accuracy of the FOWT simulations conducted in this study, a validation is carried out by comparing the aerodynamic performance with results obtained from other numerical simulations. The reference data for validation are taken from Lee and Lee, under uniform inflow conditions with a wind speed of 8 m/s. The prescribed surge motion has an amplitude of 4 m and a frequency of 0.1 Hz, while the pitch motion has an amplitude of 4° and a frequency of 0.05 Hz. Figure 6 presents the comparison of rotor thrust and power. Some discrepancies are observed, which may be attributed to the inclusion of the vertical component of gravitational force due to rotor tilt in the present simulation, as well as the limited resolution of the airfoil interpolation tables. Despite these differences, the overall aerodynamic performance shows good agreement with the reference results. These findings demonstrate the reliability of the numerical

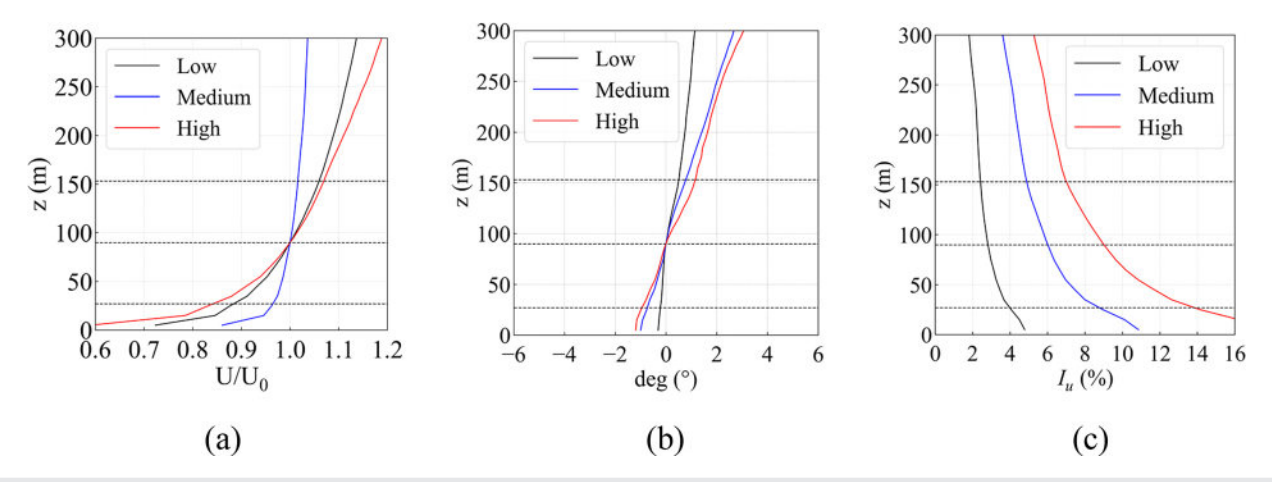


FIG. 4. The time-averaged vertical profiles: (a) wind speed, (b) wind direction, and (c) turbulence intensity.

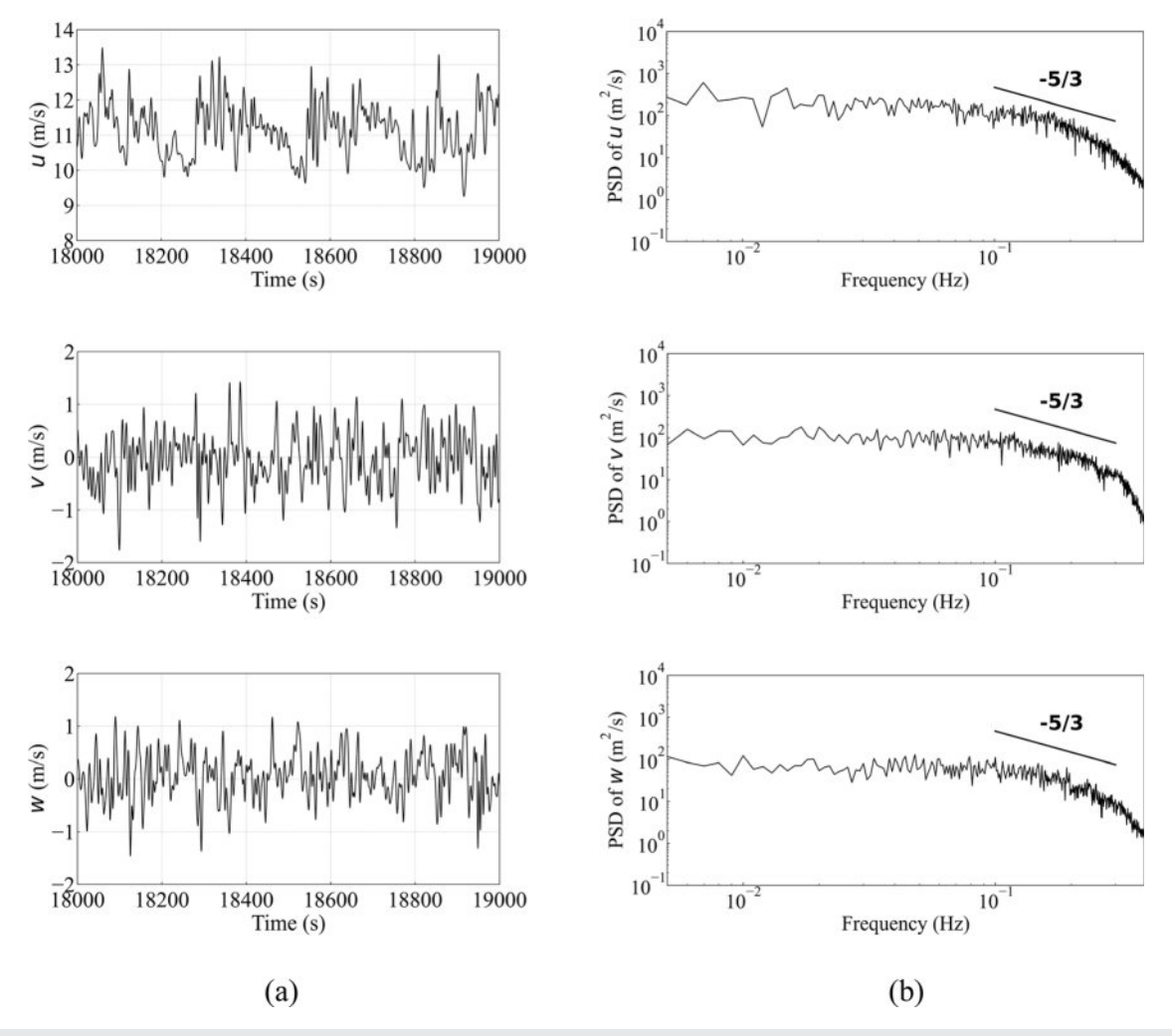


FIG. 5. The three velocity components on the xy plane at hub height: (a) time histories and (b) power spectral densities.

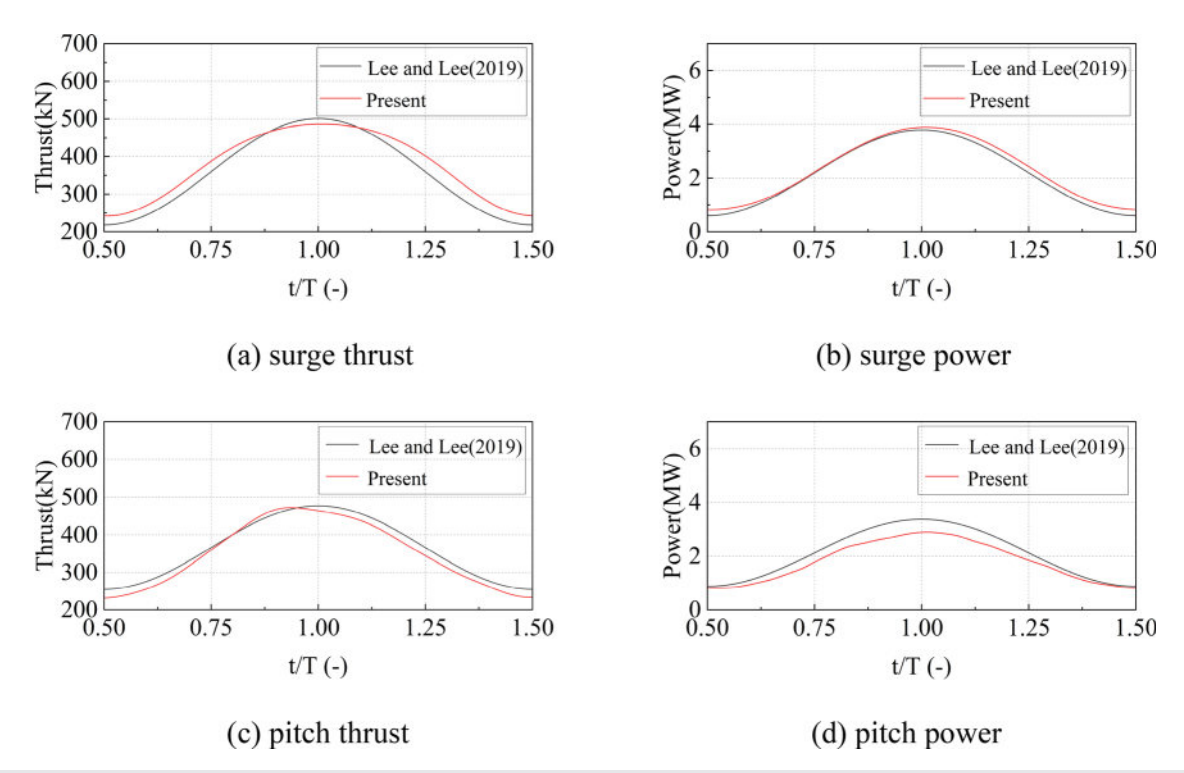


FIG. 6. Comparison of rotor thrust and power.

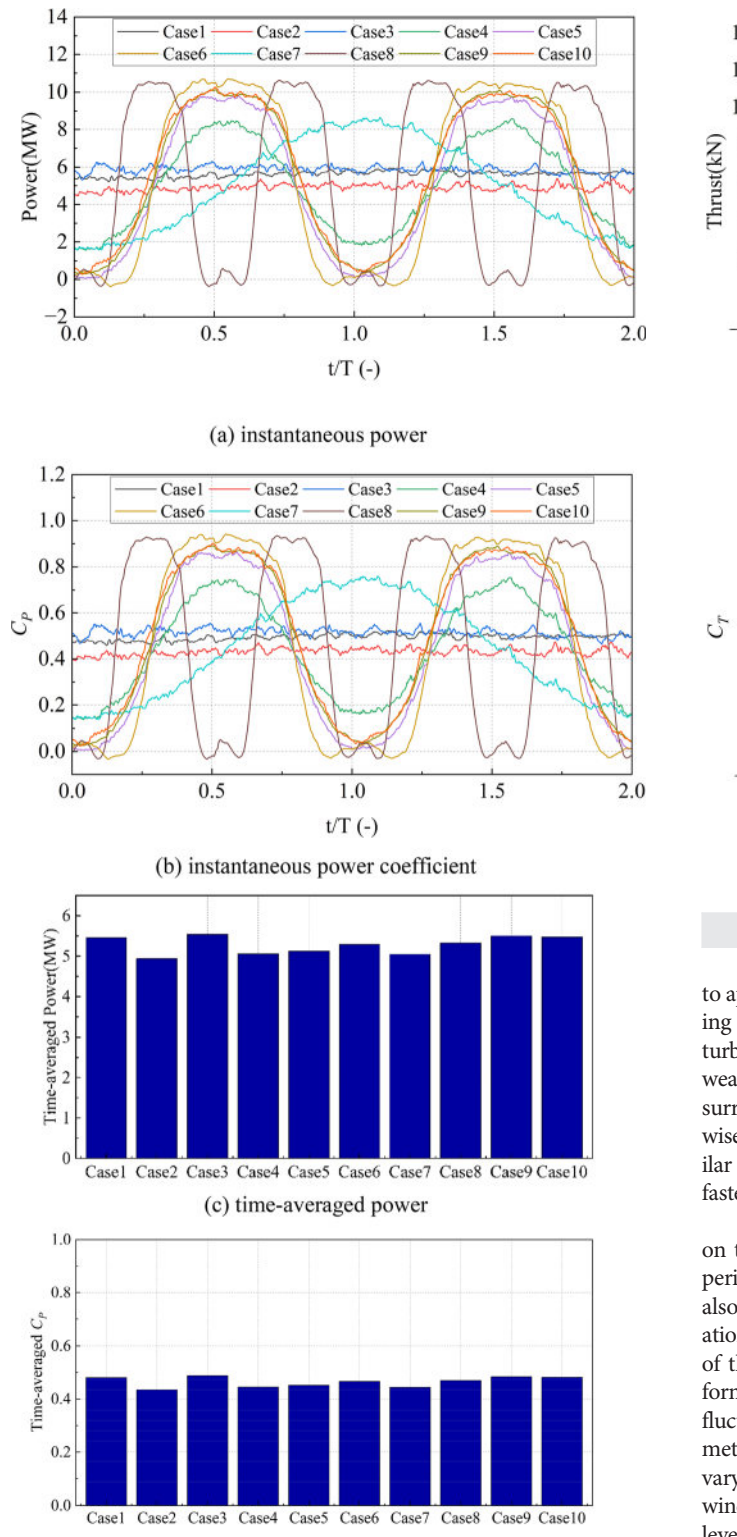
method employed in this study for subsequent investigations of the wake characteristics of floating offshore wind turbines.

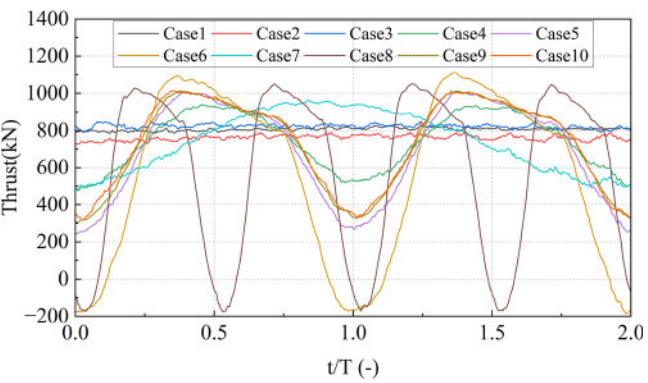
# IV. RESULTS AND DISCUSSION A. Aerodynamic performance

The aerodynamic performance of the FOWT is an intrinsic factor influencing wake characteristics, and its analysis is essential for future studies on floating wind farms. Figure 7 presents the instantaneous power variation and the time-averaged power. The non-dimensional time is normalized by the period of the reference case, which is 10 s. It should be noted that the time-averaged power is calculated over the entire 600 s dataset. Figure 8 shows the instantaneous thrust variation. For clarity, the corresponding power and thrust coefficients are also shown in Figs. 7 and 8. The results indicate that platform motion has a limited effect on the time-averaged power, with the power output of the FOWT being slightly higher than that of the FBWT under certain conditions. The trends of instantaneous power and thrust are consistent. For the FBWT, fluctuations are observed within a certain range due to the presence of atmospheric turbulence. In contrast, the platform motion of the FOWT significantly intensifies these fluctuations. The fluctuation frequency matches the platform motion frequency, and higher motion amplitudes and frequencies lead to larger oscillations in power and thrust. In addition, it is observed that in some cases, the instantaneous power and thrust briefly reach negative values. This occurs when the FOWT experiences relatively large downstream motion velocities, which may cause the turbine to inject energy into the flow field. This phenomenon is known as the propeller state. 11,12,41 When the platform motion velocity exceeds the incoming wind speed, the FOWT can enter the propeller state. <sup>41</sup> In this state, the turbine no longer extracts kinetic energy from the inflow but instead imparts momentum to it, functioning in a manner similar to a propeller. Simple rotor-speed and pitch control cannot prevent this phenomenon, as discussed further in Appendix A. In practice, however, advanced control strategies can effectively suppress platform motions <sup>42</sup> and thereby avoid the occurrence of this state. Nevertheless, in the present simulations, the negative thrust appears only transiently within part of a motion cycle, while the wake still exhibits coherent structures and physically meaningful flow features under these extreme motion conditions. In summary, platform motion has a significant influence on the aerodynamic performance of the FOWT.

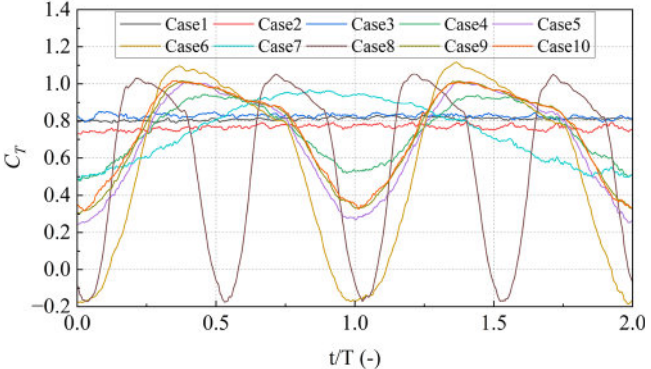
# B. Wake velocity deficit characteristics

This subsection presents the characteristics of wake velocity deficit. Figure 9 shows contour plots of the streamwise velocity on the horizontal plane at hub height. The left column displays the instantaneous streamwise velocity at the final time step, while the right column presents the time-averaged streamwise velocity. From the instantaneous streamwise velocity contours, it can be observed that, compared to the FBWT cases, platform motion induces periodic fluctuations in the wake region, which are particularly pronounced in the shear layer. The extent of this fluctuation is influenced by the amplitude and frequency of the motion, as well as the ambient turbulence intensity. Larger motion amplitudes and higher frequencies lead to a wider affected region, while lower ambient turbulence intensities also enhance the influence range. For the case with a turbulence intensity of 6.02%, the fluctuation effect extends downstream









(b) instantaneous thrust coefficient

FIG. 8. Instantaneous thrust performance.

to approximately 4D. However, for all cases, significant wake meandering is observed in the far-wake region (x>4D) due to atmospheric turbulence. In this region, the influence of platform motion is relatively weakened, and the wake development is primarily governed by the surrounding turbulent environment. From the time-averaged streamwise velocity contours, it can be observed that the wake shapes are similar across different cases; however, the wake recovery is generally faster under FOWT cases.

Figure 10 shows the instantaneous streamwise velocity contours on the vertical plane through the rotor center. The results show that periodic fluctuations similar to those observed on the horizontal plane also appear on the vertical plane. However, it is evident that the fluctuations in the upper part of the wake are more regular. The periodicity of the shear layer fluctuations appears to be correlated with the platform motion frequency. In contrast, in the lower part of the wake, the fluctuations exhibit significantly more irregular patterns. This asymmetry in fluctuation patterns may be attributed to both the vertically varying effect of pitch motion and the stratification introduced by wind shear. This phenomenon may lead to more complex ground-level interactions and further increase the complexity of the near-ground wake behavior.

To quantify the velocity differences, the disk-averaged streamwise velocity  $u_{\text{disk}}$ , defined as the time- and disk-averaged streamwise

(d) time-averaged power coefficient

FIG. 7. Power performance

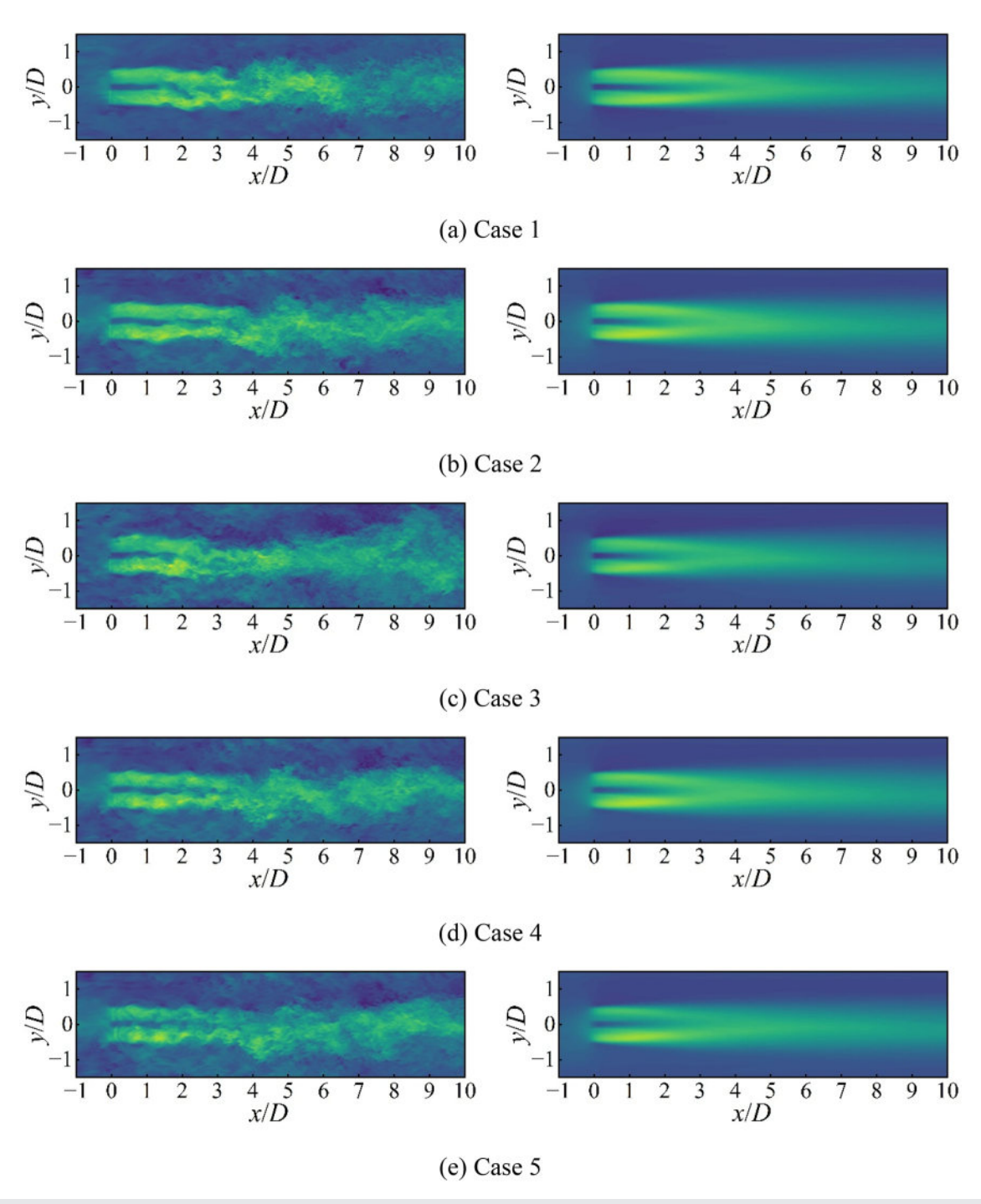
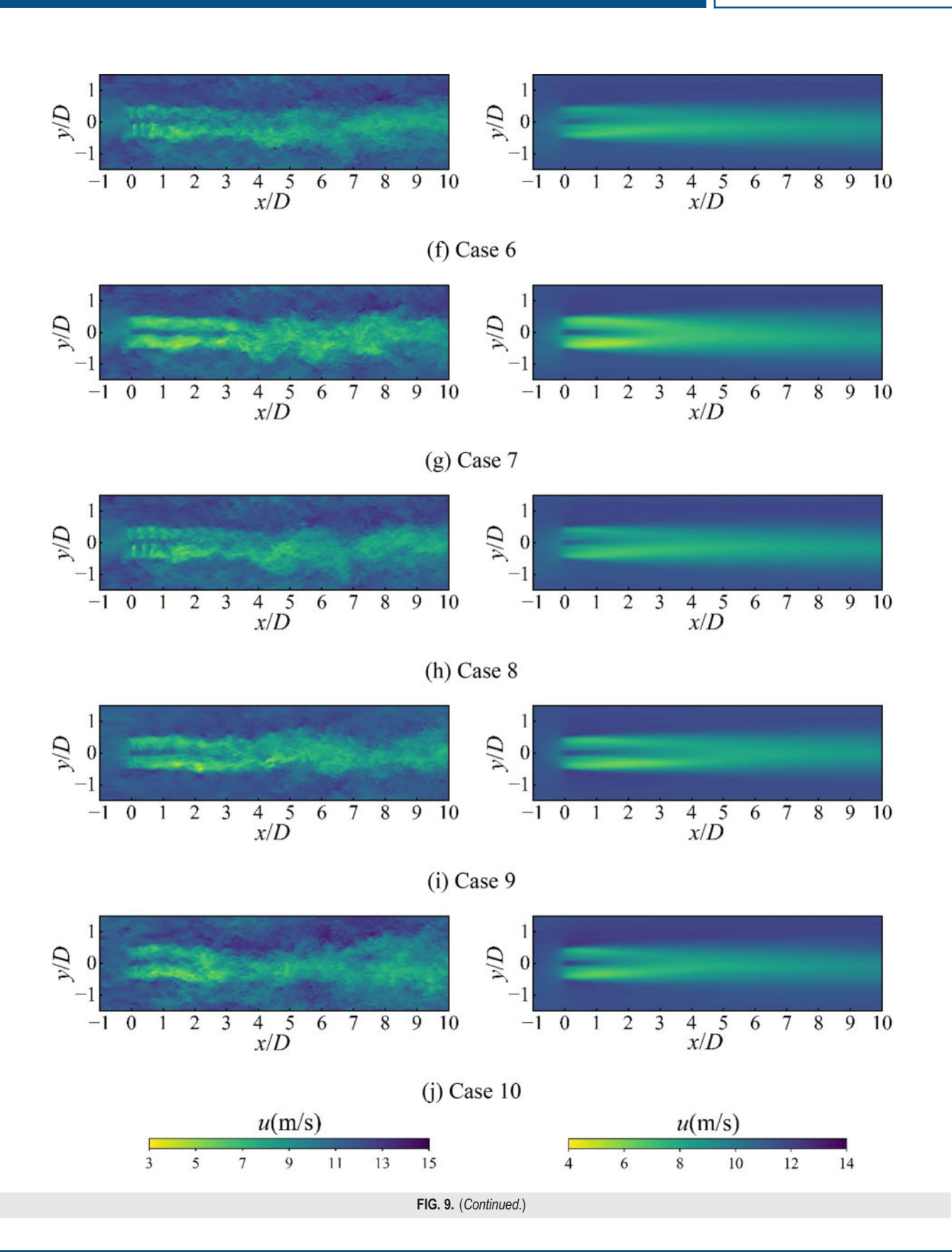


FIG. 9. The streamwise velocity on the horizontal plane at hub height.

velocity on yz planes located at various downstream distances, is extracted. Table IV presents the ratio of  $u_{\rm disk}$  between the FOWT and the corresponding FBWT under the same inflow conditions. The results show that, compared to the FBWT, the FOWT generally

exhibits an increase in  $u_{\rm disk}$ , with a maximum enhancement of 18.32% observed in the near-wake region. As the downstream distance increases, the velocity recovery becomes increasingly dominated by atmospheric turbulence, while the influence of platform motion



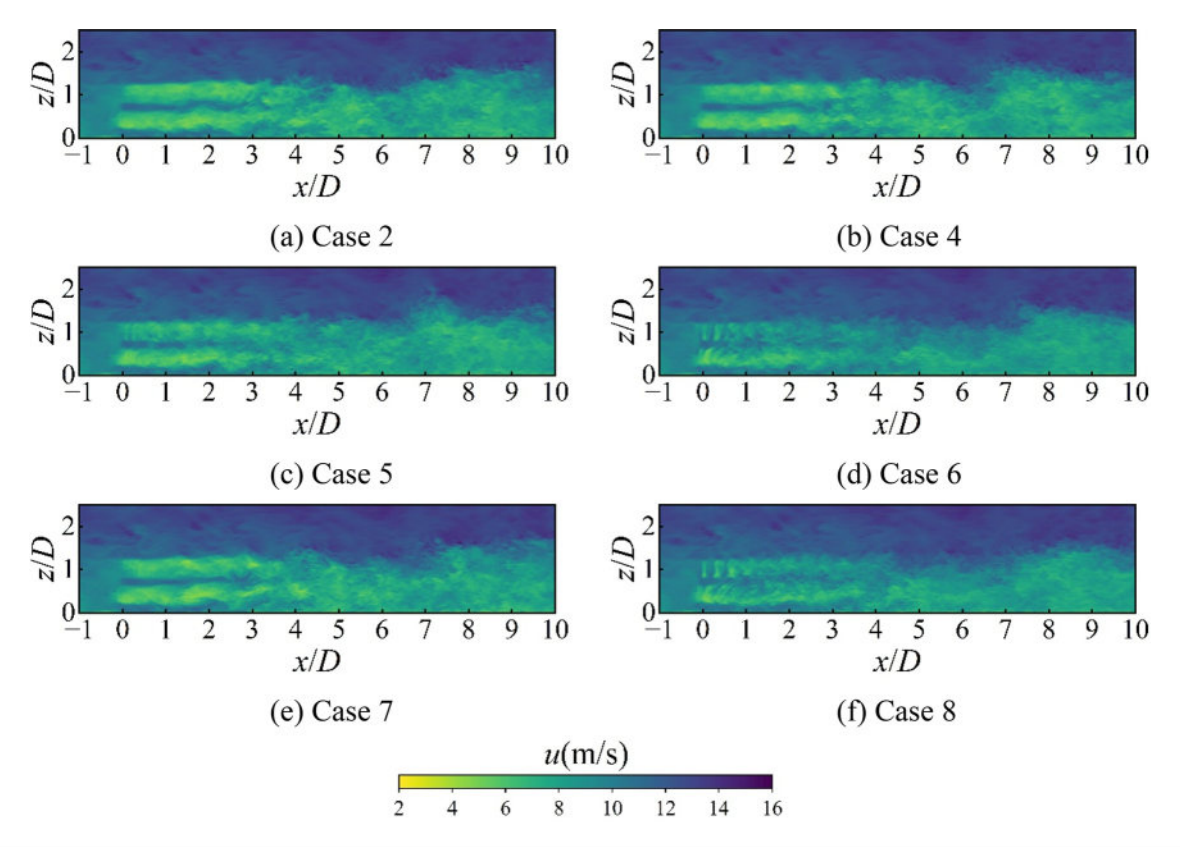


FIG. 10. The instantaneous streamwise velocity contours on the vertical plane through the rotor center.

**TABLE IV.** The ratio of  $u_{disk}$  between the FOWT and the corresponding FBWT.

	Case 4	Case 5	Case 6	Case 7	Case 8	Case 9	Case 10
x/D=3	101.69%	106.89%	118.32%	102.45%	116.91%	108.91%	107.02%
x/D = 4	100.93%	104.60%	113.14%	101.92%	111.99%	105.49%	104.87%
x/D = 5	100.40%	103.01%	109.51%	101.25%	108.51%	103.32%	103.46%
x/D = 6	100.08%	101.96%	107.24%	100.76%	106.32%	101.82%	102.53%
x/D = 7	99.87%	101.22%	105.68%	100.31%	104.82%	100.87%	101.75%
x/D = 8	99.87%	100.77%	104.52%	99.97%	103.66%	100.29%	101.09%

gradually diminishes. Beyond 5D downstream, the increase in  $u_{\rm disk}$  drops significantly for most cases, remaining below 4%. Notably, cases 6 and 8 exhibit larger increases, likely due to their higher motion amplitudes and frequencies, which induce stronger disturbances in the wake and promote faster recovery. In some cases, a slight decrease in  $u_{\rm disk}$  is observed beyond 7D, which may be attributed to stochastic perturbations from atmospheric turbulence. Furthermore, it is observed that under the same motion conditions, the influence of different turbulence intensities on this metric is relatively minor.

Figures 11 and 12 show the normalized velocity deficit profiles on the horizontal plane at hub height and the vertical plane through the rotor center, respectively, categorized by inflow turbulence intensity. The normalized velocity deficit is defined as  $(u_{hub} - u)/u_{hub}$ , where

 $u_{hub}$  is set to 11.4 m/s. This metric is used to quantitatively analyze the differences in wake recovery among different cases. In the near-wake region, the velocity deficit exhibits a double-peaked Gaussian shape. As the downstream distance increases, the wake gradually develops self-similar characteristics and transitions to a single-peaked Gaussian profile. Under atmospheric turbulence, the wake continues to expand and recover downstream, but a noticeable velocity deficit remains even at a downstream distance of 10D. The results indicate that, compared to the FBWT, platform motion significantly influences the velocity deficit, promoting faster wake recovery. This influence gradually weakens with increasing downstream distance. For cases with turbulence intensities of 2.82% and 6.02%, the effect extends up to approximately 6D downstream, whereas for the case with a turbulence intensity of 9.02%,

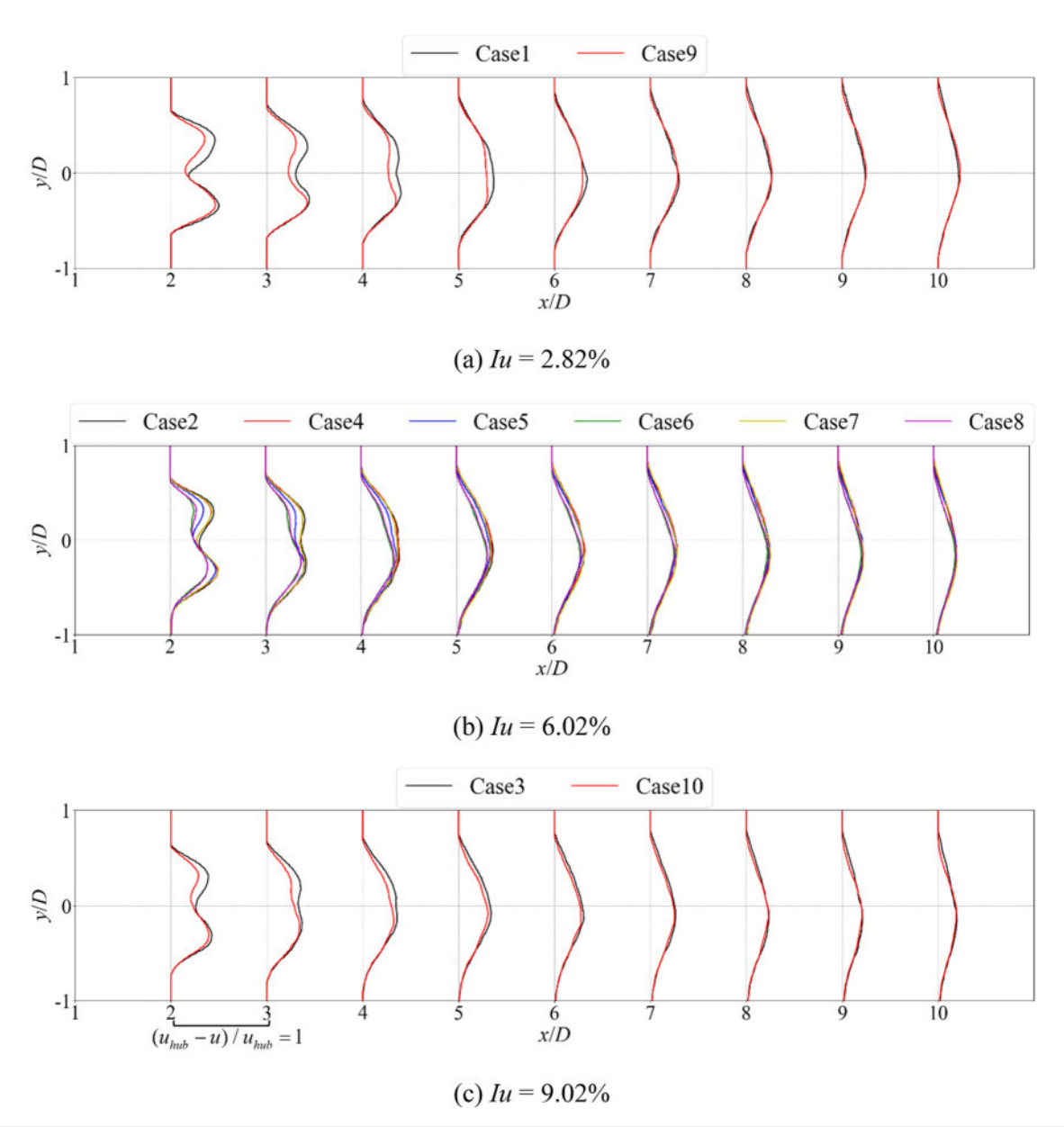


FIG. 11. The normalized velocity deficit profiles on the horizontal plane at the hub height.

the influence is substantially reduced beyond 5D. As previously observed, larger motion amplitudes and higher frequencies result in a stronger influence on wake recovery. On the horizontal plane, cases 6 and 8 exhibit maximum reductions in velocity deficit of 30.42% and 26.71%, respectively, at 5D downstream, while the reductions for other cases remain below 15%. Furthermore, on the vertical plane, more pronounced differences in velocity deficit are observed in the lower part of the wake, and these differences remain evident up to 7D downstream. This may be attributed to the more complex ground effects induced by pitch motion, which enhance wake recovery in the near-ground region.

The applicability of three representative analytical wake models under coupled surge–pitch motions is assessed. LES results serve as reference to benchmark the Jensen model<sup>43</sup> (top-hat), Bastankhah model<sup>44</sup> (Gaussian), and Zhang model<sup>45</sup> (cosine-shaped). Figure 13 presents the normalized velocity-deficit profiles on the horizontal plane at hub height obtained from the LES and different models. The Jensen model, based on the top-hat assumption, shows noticeably larger discrepancies from the LES distributions. In contrast, both the Bastankhah and Zhang models capture the wake-deficit profiles more accurately, with improved agreement at downstream positions beyond  $x/D \ge 6$ . Nevertheless, all three models inherently assume a laterally

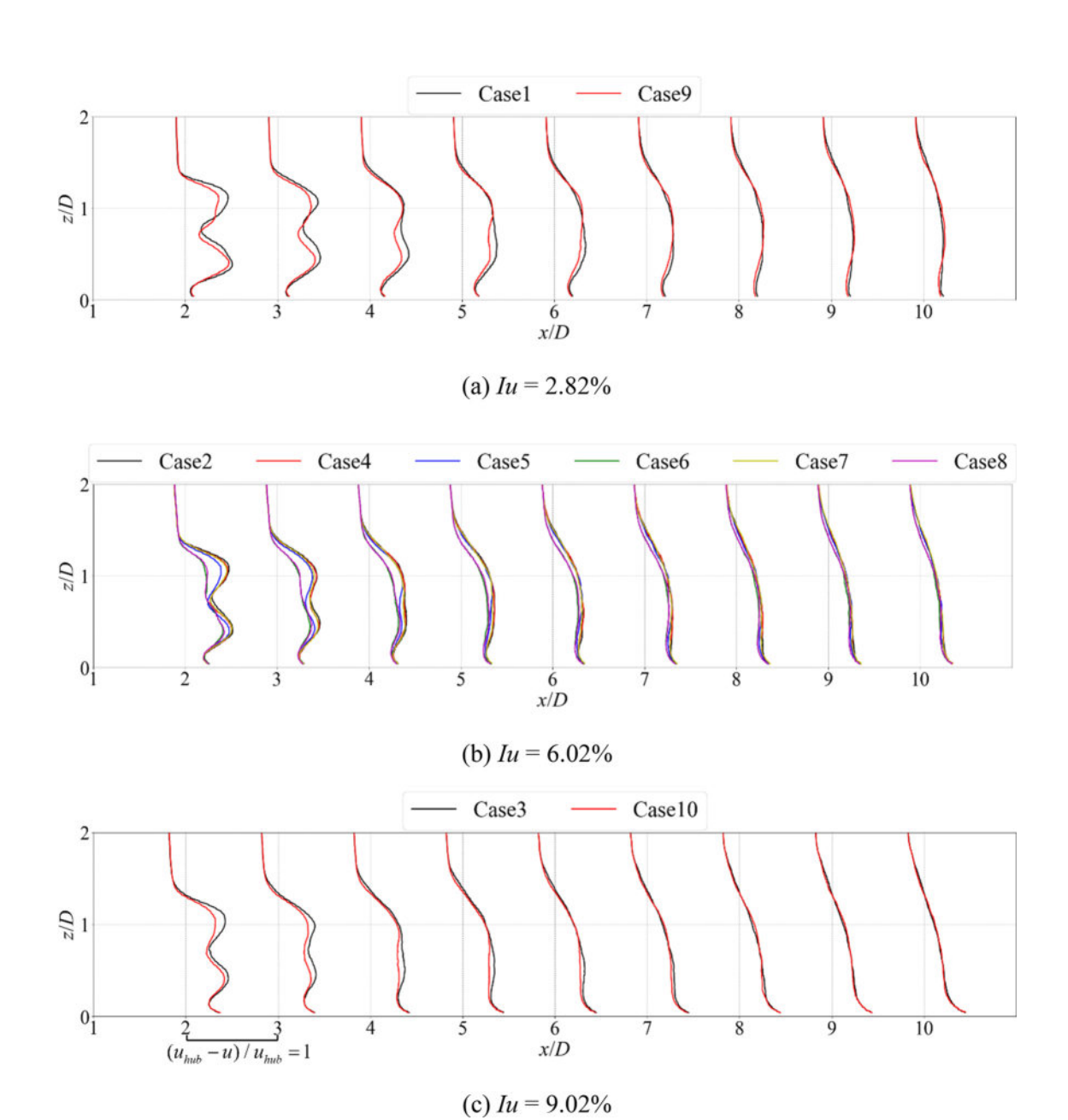
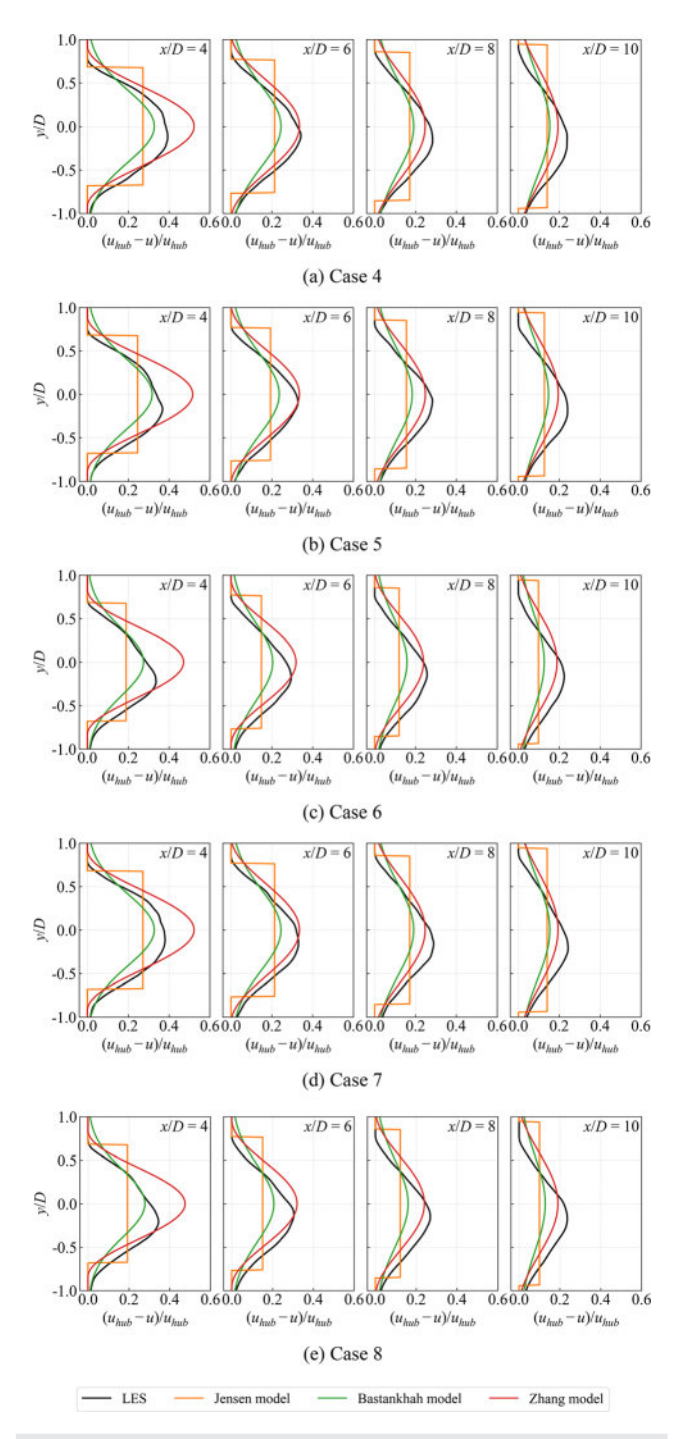


FIG. 12. The normalized velocity deficit profiles on the vertical plane through the rotor center.

symmetric wake, whereas wind veer in the ABL inflow produces an asymmetric wake. Overall, analytical wake models show certain discrepancies in predicting FOWT wakes, highlighting the need for further refinement to enhance their applicability under floating offshore conditions.

Building upon the velocity deficit profiles, Gaussian fitting is employed to extract the Gaussian standard deviation and the wake centerline position. These are key parameters in analytical wake models. In this study, the standard deviations are defined separately in the horizontal and vertical directions, following the framework of the three-dimensional wake model. Figure 14 presents the Gaussian

standard deviations in the horizontal  $(\sigma_y)$  and vertical  $(\sigma_z)$  directions, along with the corresponding wake centerline positions. The wake centerline is defined as the time-averaged wake position, determined as the location of the Gaussian peak obtained by fitting the time-averaged velocity deficit profile. The accuracy of the Gaussian fitting is discussed in Appendix B. Due to the effect of wind veer in the ABL, a certain degree of wake centerline deflection is observed. Similar trends are found in both the horizontal and vertical directions. When the platform motion amplitude and frequency are relatively small, the Gaussian standard deviations and centerline positions of the FOWT wake are generally consistent with, or slightly lower than, those of the



**FIG. 13.** The normalized velocity deficit profiles on the horizontal plane at the hub height obtained from the LES and different models.

FBWT. However, as the platform motion becomes more pronounced, evident in the results of cases 6 and 8, the Gaussian standard deviations decrease significantly, the horizontal wake centerline deviates further from the centerline, and the vertical centerline shifts closer to the hub

height. The reduction in Gaussian standard deviation reflects a more concentrated wake core, which is likely caused by the periodic compression of wake structures resulting from the platform motions. This periodic oscillation reduces lateral expansion, leading to a smaller  $\sigma$ , while the large-scale coherent structures may simultaneously enhance the entrainment of high-momentum fluid into the wake core, thereby accelerating the velocity recovery despite the more concentrated wake profile. In contrast, the deviation of the wake centerline may be attributed to the stronger platform motions, which generate more pronounced unsteady aerodynamic forces and thereby enhance wake asymmetry.

Figures 15 and 16 present the streamwise turbulence intensity profiles on the horizontal plane at hub height and the vertical plane through the rotor center, respectively, for different inflow turbulence intensities. The turbulence intensity in the wake is denoted as  $I_{wake}$ . The results show that the differences between FOWT and FBWT are relatively small, with the FOWT exhibiting slightly lower turbulence intensity in the wake region. This may be attributed to the background ABL inflow, which already contains substantial turbulent kinetic energy and, therefore, limits the additional effect of platform motion on turbulence generation. The platform-induced oscillations promote cross-stream and vertical mixing, which accelerates the homogenization of the wake but simultaneously reduces mean shear, thereby lowering turbulence production. The observations, thus, provide indirect evidence that the faster wake recovery of the FOWT arises mainly from large-scale coherent structures induced by the platform motion, rather than from an increase in wake turbulence.<sup>18</sup> Moreover, the lower turbulence intensity in the FOWT wake also helps explain its smaller Gaussian standard deviation: weaker turbulence reduces lateral diffusion, leading to a more concentrated wake core. This interpretation is consistent with the earlier analysis, where the reduction in the standard deviation is attributed to the periodic compression of wake structures by the platform motions.

# C. Wake vorticity structure

This subsection presents the wake vorticity structures. The vorticity field is defined as the curl of the velocity field,  $\omega = \nabla \times \vec{U}$ , where  $\vec{U}$  denotes the velocity vector. In this study, the vorticity distributions are analyzed on the horizontal plane at hub height and the vertical plane through the rotor center, focusing on the dominant rotational component for each plane.

Figure 17 presents the instantaneous vorticity fields on the horizontal plane at the hub height and the vertical plane through the rotor centerline. The instantaneous vorticity fields reveal that in the far-wake region, both cases exhibit pronounced wake meandering. In the near-wake region, the FBWT case shows relatively smoother and more symmetric vortex structures, whereas the FOWT case displays periodic undulations in the shear layers, likely induced by the platform motion. These features are consistent with the patterns observed in the instantaneous velocity fields discussed earlier.

To further investigate the influence of platform motion on the vortex structures, phase-averaged vorticity fields are computed based on the motion period of each case. Specifically, the instantaneous vorticity fields at the same phase position are extracted and averaged over multiple motion cycles to filter out random turbulent fluctuations and retain coherent, motion-induced features. In this study, the results

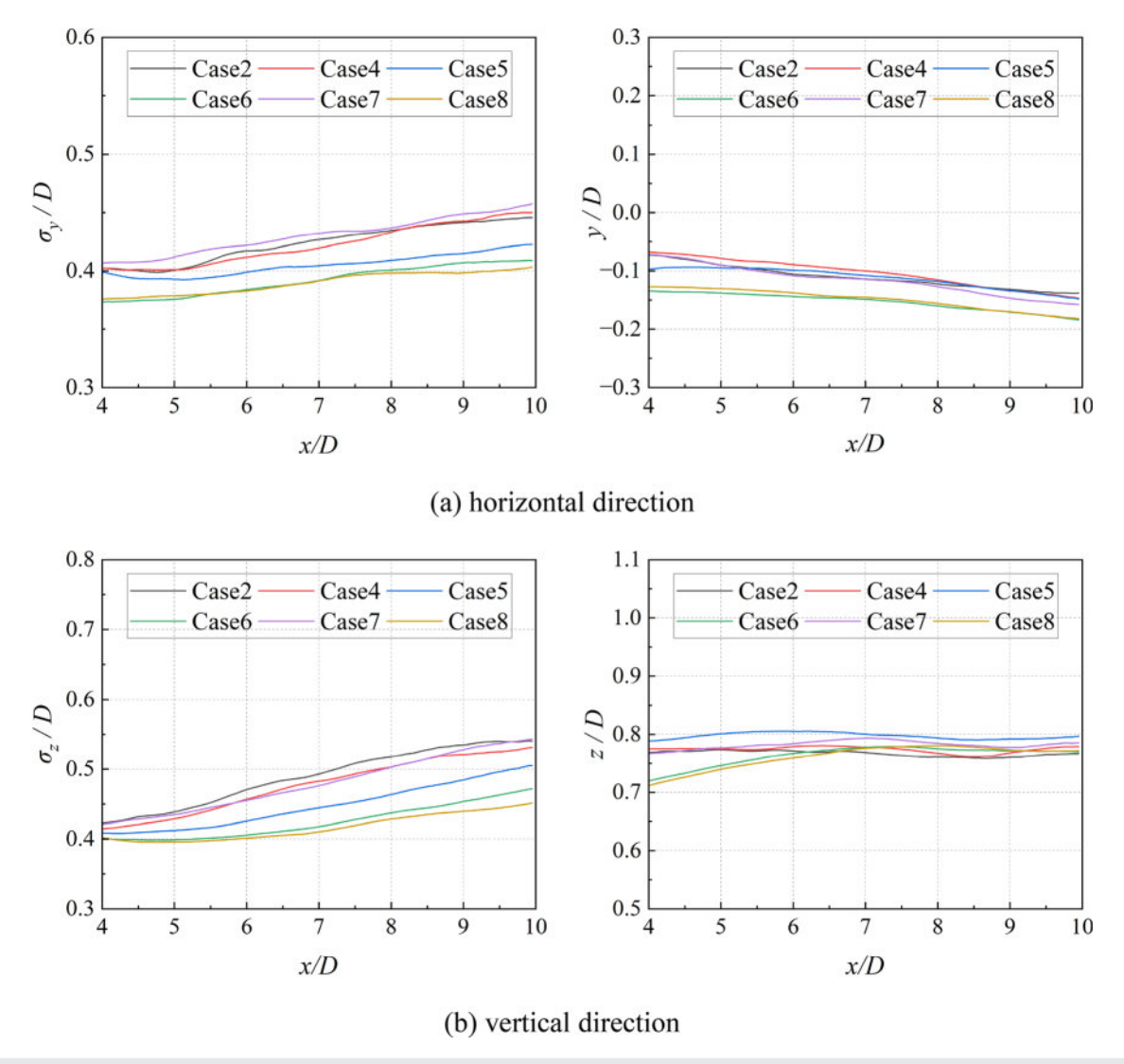


FIG. 14. The Gaussian standard deviations and wake centerline positions.

corresponding to the first phase instant are selected for analysis. Figure 18 presents the phase-averaged vorticity fields on the horizontal plane at the hub height. The phase-averaged results indicate that elevated vorticity is primarily concentrated in the near-wake region, corresponding to the zones where tip and root vortices are shed. Under the influence of atmospheric turbulence, the coherence of these vortices gradually decays downstream, and their interactions contribute to the formation of large-scale vortex structures within the shear layer. As the turbulence intensity increases, this transition occurs closer to the wind turbine. For FBWTs, this phenomenon can be observed approximately 3-4D downstream. Unlike the relatively smooth shear-layer structures seen in FBWTs, the wake of FOWTs undergoing combined surgepitch motion exhibits pronounced periodic vortex structures, particularly evident in the shear layer region, which is consistent with the findings of Li et al. 18 These periodic structures are closely related to the platform motion; the relative motion of the rotor over a motion cycle

modulates the shedding of tip vortices, leading to their periodic merging and the formation of periodically distributed vortical patterns along the shear layer. 18 Comparisons among different cases reveal that the periodic vortex structures are highly sensitive to the platform motion frequency: higher frequencies lead to more compact structures, while larger motion amplitudes result in stronger fluctuations within the shear layer. In addition, platform motion accelerates the decay of coherence in the tip and root vortices, promoting earlier interactions with the surrounding flow. In cases 6 and 8, this transition is observed downstream of 3D, potentially enhancing momentum exchange between the wake and the ambient flow and facilitating faster recovery of the velocity deficit. A comparison across different ambient turbulence intensities shows that atmospheric turbulence exerts a noticeable suppressing effect on the platform-induced periodic vortex structures. Under low turbulence intensity conditions, these periodic structures can be clearly observed up to 4D downstream near the shear layer.

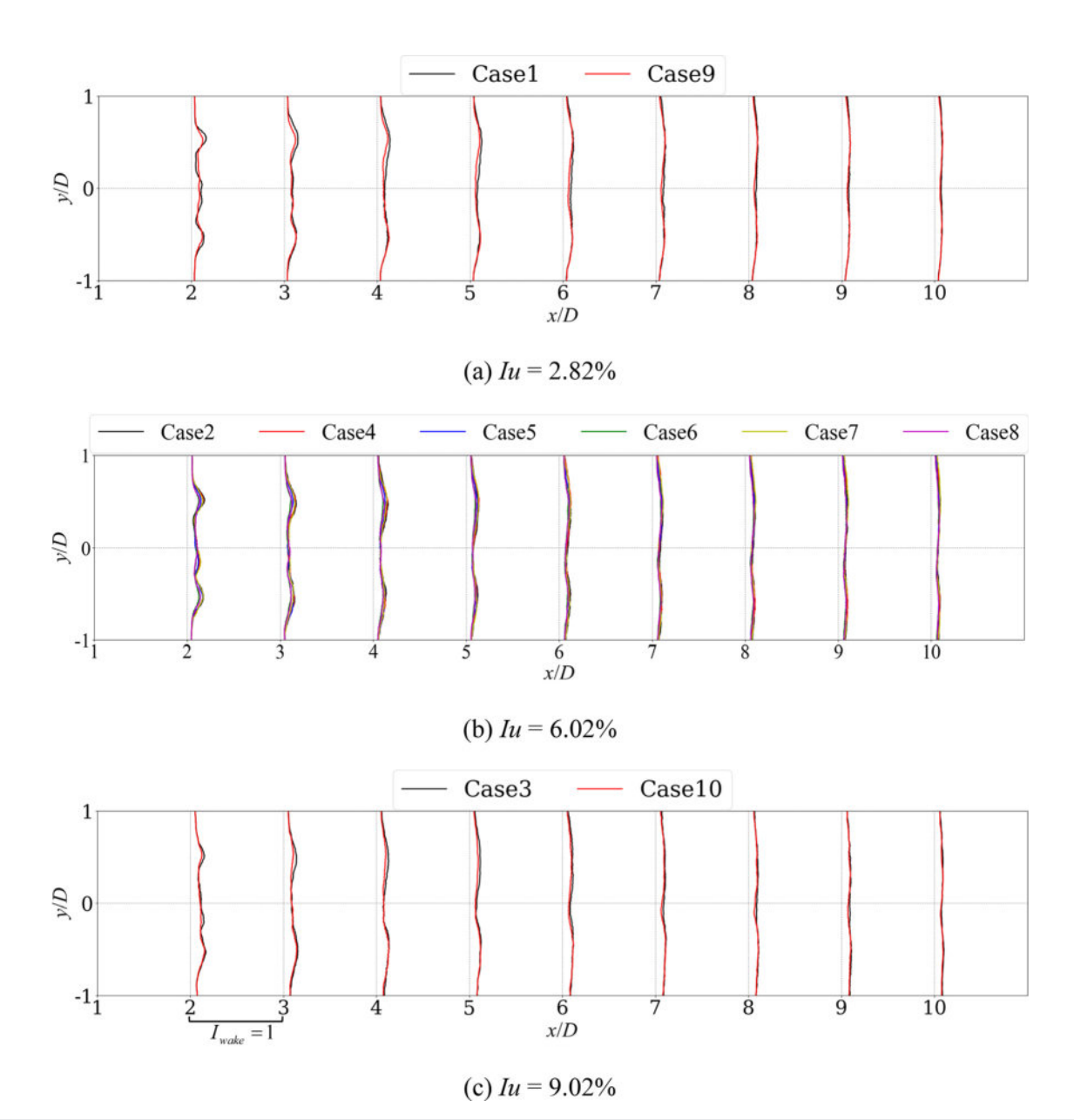


FIG. 15. The turbulence intensity profiles on the horizontal plane at hub height.

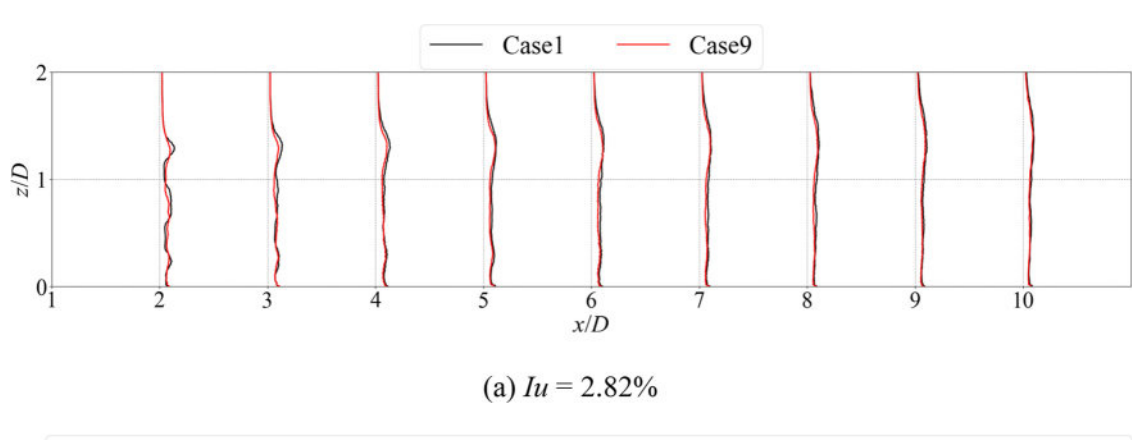
However, under high turbulence intensity, they are only distinguishable within 3D downstream.

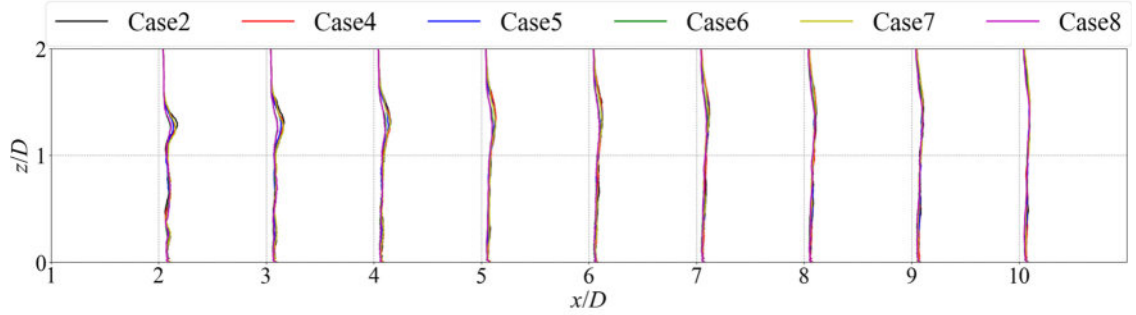
Figure 19 presents the phase-averaged vorticity field on the vertical plane through the rotor center. The results show that, compared to the horizontal plane, higher vorticity magnitudes are observed near the ground. This may be attributed to the enhanced vertical disturbances induced by platform pitch motion, which intensify vortex mixing within the shear layer and lead to localized vorticity amplification. Additionally, in the far-wake region of the vertical plane, the vorticity streaks near the ground gradually weaken and eventually disappear, whereas those farther from the ground persist over longer downstream

distances. This asymmetry may be related to stronger shear layer dissipation near the surface, as well as further amplified by wake deflection induced by platform pitch motion. Despite these local differences, the overall modulation patterns of vortex structures caused by platform motion on the vertical plane are consistent with those observed on the horizontal plane.

## D. Dynamic mode analysis of wake evolution

The wake structure of FOWTs is influenced by multiple perturbations, including blade rotation, platform motion, and atmospheric







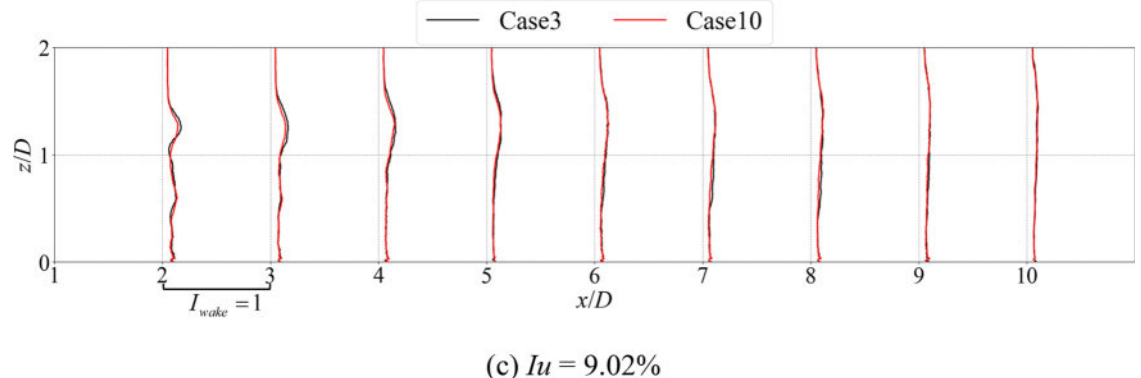


FIG. 16. The turbulence intensity profiles on the vertical plane through the rotor center.

turbulence, resulting in complex spatiotemporal evolution characteristics. Among various analytical approaches, modal decomposition has proven to be a powerful tool for uncovering dominant flow structures and their dynamic behavior in unsteady flows. In this study, the dynamic mode decomposition (DMD) method<sup>48</sup> is employed to further elucidate the spatiotemporal evolution of FOWT wakes, which enables the extraction of coherent spatial structures associated with specific frequencies from unsteady flow fields.

The DMD method represents the unsteady flow field as a linear combination of dynamic modes, each associated with a specific

frequency and spatial structure. The reconstructed flow field u(x,t) can be written as

$$u(x,t) \approx \sum_{k=1}^{n} \phi_k(x) \exp(\omega_k t) b_k = \sum_{k=1}^{n} \phi_k(x) \lambda_k^{(t/\Delta t)} b_k, \quad (10)$$

where  $\phi_k(x)$  represents the kth spatial mode,  $\lambda_k$  is the associated complex eigenvalue encoding growth/decay and frequency information,  $b_k$  is the mode amplitude, and  $\Delta t$  is the temporal sampling interval. The modal energy is defined as the squared mode amplitude, and the

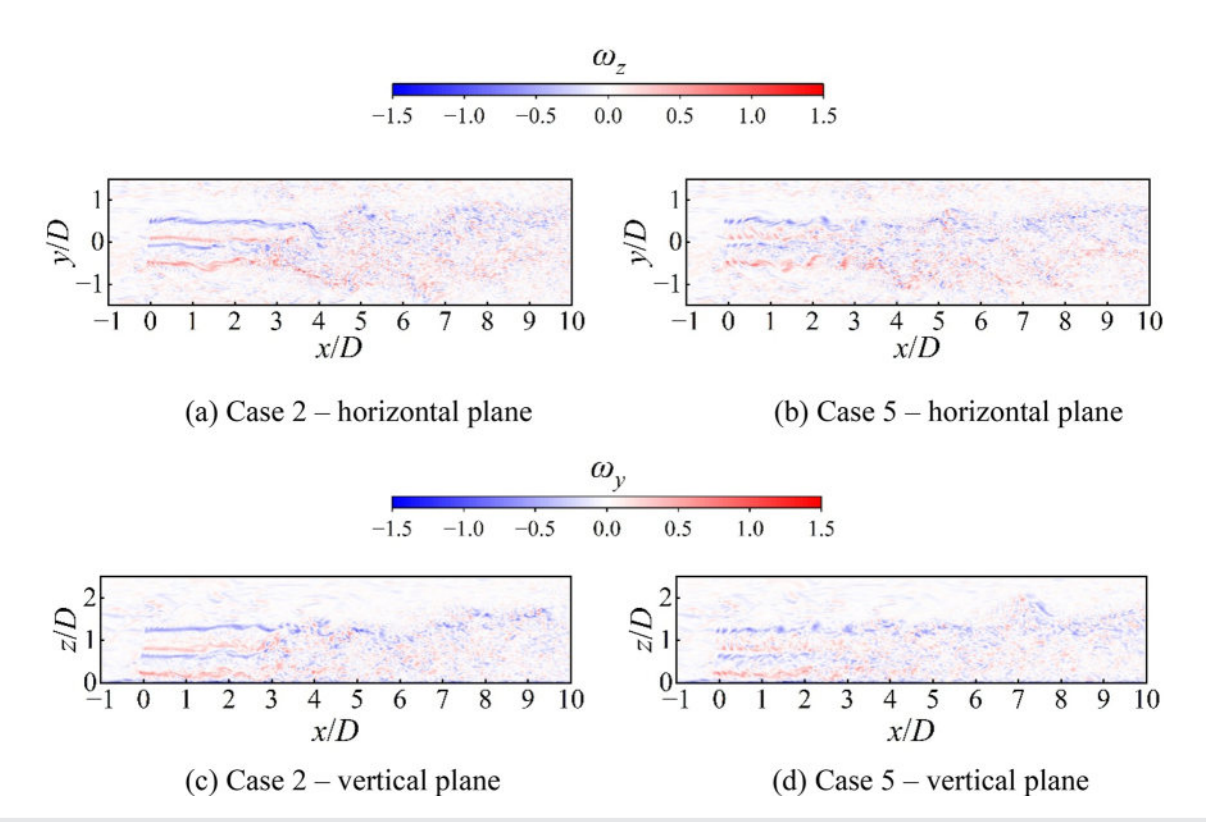


FIG. 17. The instantaneous vorticity fields.

reconstruction error is quantified by the normalized  $L_2$ -norm difference between the LES and DMD-reconstructed signals. In this study, the last 600 s of simulation data are used for DMD analysis, which is performed on the streamwise velocity component, with a temporal sampling interval of 0.2 s, resulting in a total of 3000 snapshots. The truncation rank is set to 500. Further details on the sampling sensitivity and reconstruction accuracy are provided in Appendix C.

Figure 20 shows the distribution of DMD eigenvalues in the complex plane for both FBWT and FOWT cases. The black circle denotes the unit circle. In the complex plane representation of DMD eigenvalues, modes located inside the unit circle correspond to decaying dynamics and are considered temporally stable, while those outside the circle exhibit growth and are regarded as temporally unstable. Eigenvalues on the unit circle indicate purely oscillatory behavior without growth or decay. For both the FBWT and FOWT cases, nearly all DMD modes are located within the unit circle, indicating that the associated flow structures are temporally stable. It should be noted that although a large number of modes are shown in the eigenvalue distribution, many of them exhibit low modal energy and may primarily reflect numerical noise or lack physical significance. Therefore, the following analysis focuses on dominant modes with relatively high energy contributions, which are more representative of coherent flow dynamics.

The DMD decomposition yields modes associated with different oscillation frequencies. The eigenvalues and corresponding modes appear in complex conjugate pairs, such that positive and negative frequency modes have symmetric spatial structures and equal modal energy. Therefore, to avoid redundancy, only the positive frequency

modes are shown and analyzed in this study. In addition, the mode with the highest energy is typically the zero-frequency mode, which corresponds to a static flow structure resembling the time-averaged flow field. This mode often dominates the overall flow field due to its strong spatial coherence. Since the time-averaged flow field has already been analyzed in Sec. IV B, and the focus of this study is on the unsteady wake dynamics induced by platform motion, the following analysis concentrates on the unsteady modes. Note that in this study, "unsteady modes" refer to non-zero-frequency modes associated with time-varying structures, distinct from the "stable" or "unstable" classification based on eigenvalue magnitude. Accordingly, the mode indices presented in this section start from mode 1, with mode 0 referring to the zero-frequency mode.

To evaluate the modulation effect of background atmospheric turbulence on wind turbine wakes, DMD analysis is first applied to an ABL flow field without the presence of a wind turbine. This case corresponds to the ABL flow with a turbulence intensity of 6.02%, and the simulation settings and sampling approach remain consistent with those used for the wind turbine cases. Figure 21 shows the DMD modes on the horizontal plane, where *f* denotes the frequency associated with each mode. The values in the contour plots represent the real part of each DMD mode. The analysis indicates that the first eight modes account for the majority of the total energy, and all dominant modes exhibit frequencies below 0.035 Hz, revealing the presence of prominent low-frequency coherent structures in the flow. From the spatial distributions of the modes, it is evident that large-scale coherent structures spontaneously form in the atmospheric turbulence and

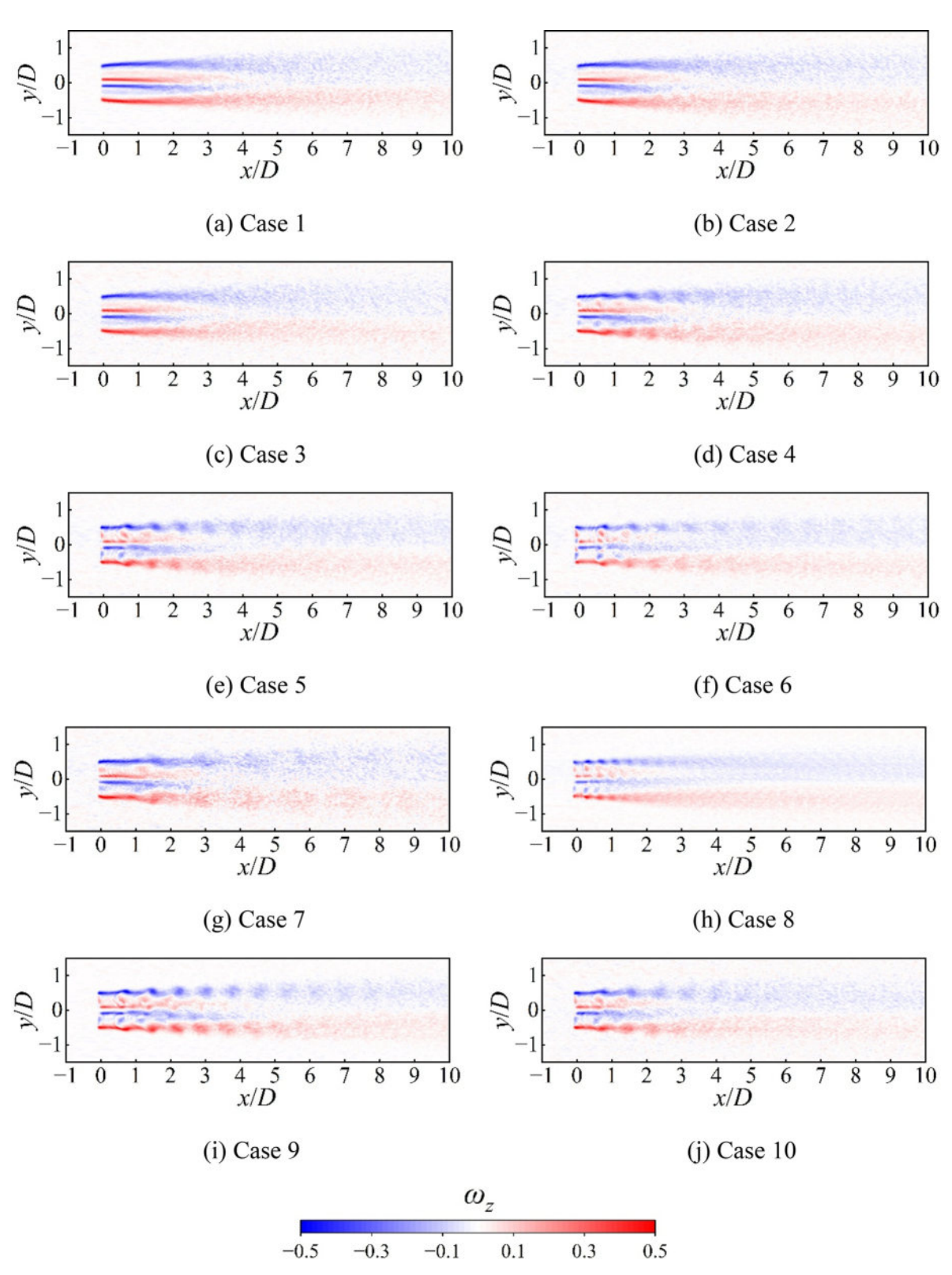


FIG. 18. The phase-averaged vorticity fields on the horizontal plane at the hub height.

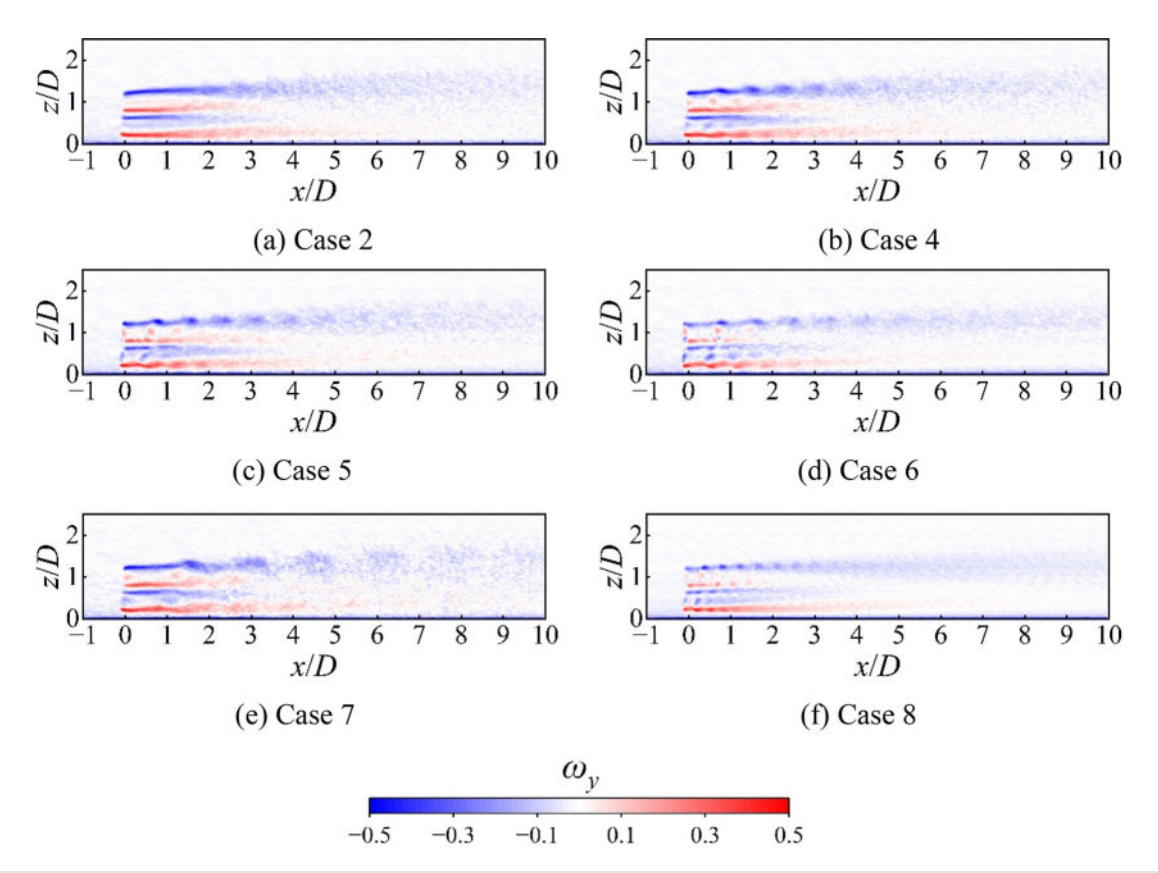
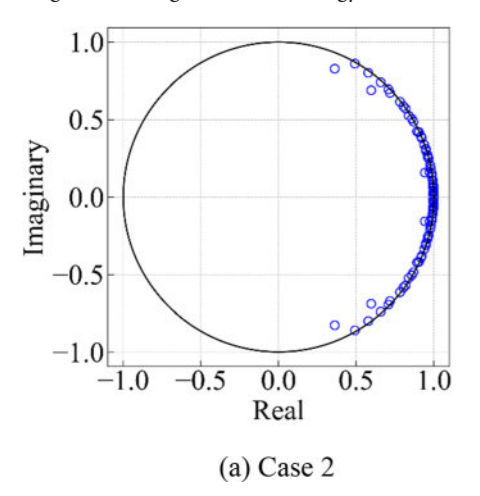


FIG. 19. The phase-averaged vorticity fields on the vertical plane through the rotor center.

alternately appear along the streamwise direction, reflecting characteristics of low-frequency disturbances.

In the DMD analysis of wind turbine cases, this study extracts the top 30 modes ranked by energy. These modes collectively account for over 99% of the total energy, with the reconstruction error of the flow field based on these modes remaining below 7%. Figure 22 presents the first eight DMD modes of case 2 on the horizontal plane at hub height. In the figure, relative energy denotes the ratio of each mode's

energy to the total energy of unsteady modes, excluding the energy of the zero-frequency mode. It is noted that DMD directly yields mode amplitudes, and modal energy is obtained as the square of the amplitude. The results show that the dominant mode frequencies in the FBWT case are all below 0.035 Hz, corresponding to a Strouhal number of approximately 0.38. Accordingly, most of these modes fall within the typical range associated with wake meandering induced by shear-layer instability, 14 while a few lower-frequency modes may



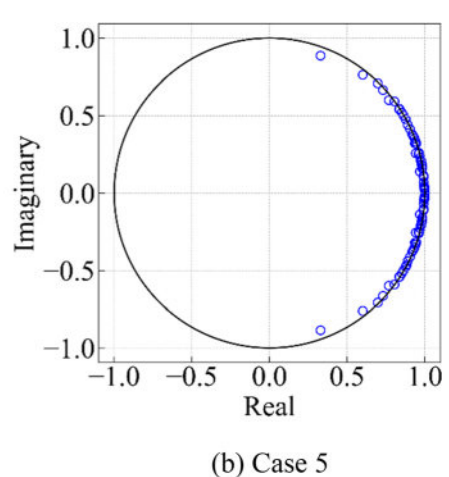


**FIG. 20.** The distribution of DMD eigenvalues in the complex plane.

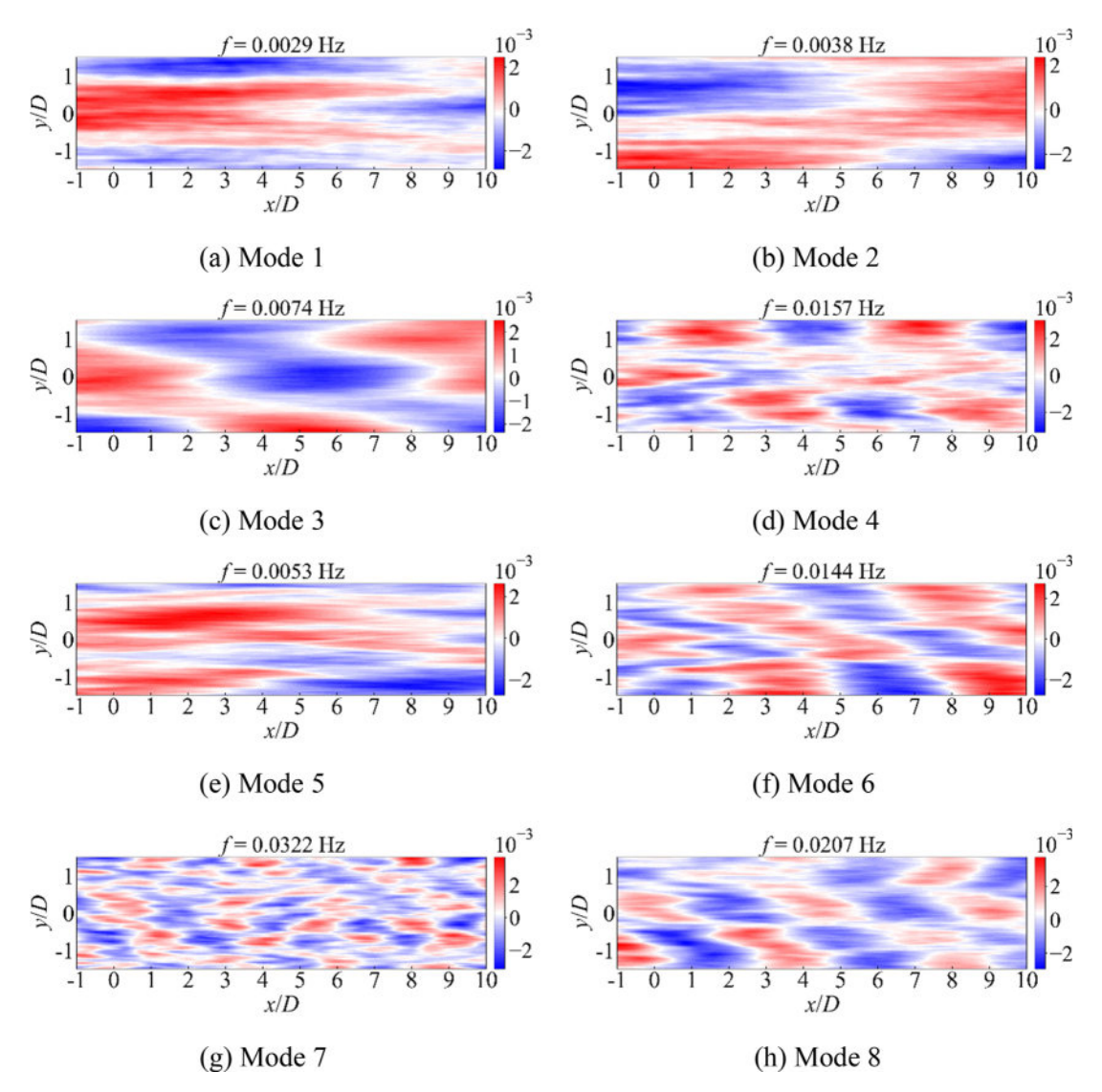


FIG. 21. The DMD modes of the ABL flow field on the horizontal plane at the hub height.

instead reflect frequencies originating from the background turbulent inflow. Modes 1–2 exhibit frequencies and spatial structures similar to those of the corresponding ABL modes, consistent with the findings of De Cillis *et al.*, <sup>24</sup> indicating that the background atmospheric turbulence exerts a significant influence on the unsteady modes within the wind turbine wake. This suggests that the unsteady modal structures in the wake are strongly modulated by the incoming turbulence. In modes 3–8, in addition to coherent structures inherited from the ABL, wake features induced directly by the turbine become increasingly evident. Specifically, mode 3 reveals a spatial distribution along the shear layer boundary in the near-wake region, possibly associated with shear layer instabilities. Mode 5 displays a localized region of strong perturbation near the turbine, implying that DMD captures turbine-induced disturbances, such as rotor rotation at this frequency. Modes 4 and 6–8 exhibit a lateral oscillation pattern in the downstream wake,

characteristic of wake meandering behavior. It is worth noting that although there are similarities in the unsteady modes between the FBWT and ABL cases, their time-averaged flow fields differ significantly. This suggests that the mean structures primarily reflect the turbine-induced modulation of the flow, while the unsteady modes preserve the coherent features originating from the incoming turbulent flow.

Figure 23 presents the first eight DMD modes of case 5 on the horizontal plane at hub height. Compared to the FBWT case, both the frequencies and spatial structures of the leading modes in the FOWT case exhibit noticeable differences. Specifically, modes 2 and 8 exhibit higher frequencies and more pronounced wake instability characteristics in their spatial patterns. Modes 4 and 7 exhibit clearer features associated with the shear layer structure. As discussed earlier, platform motion alters the time-averaged flow field structure, which serves as

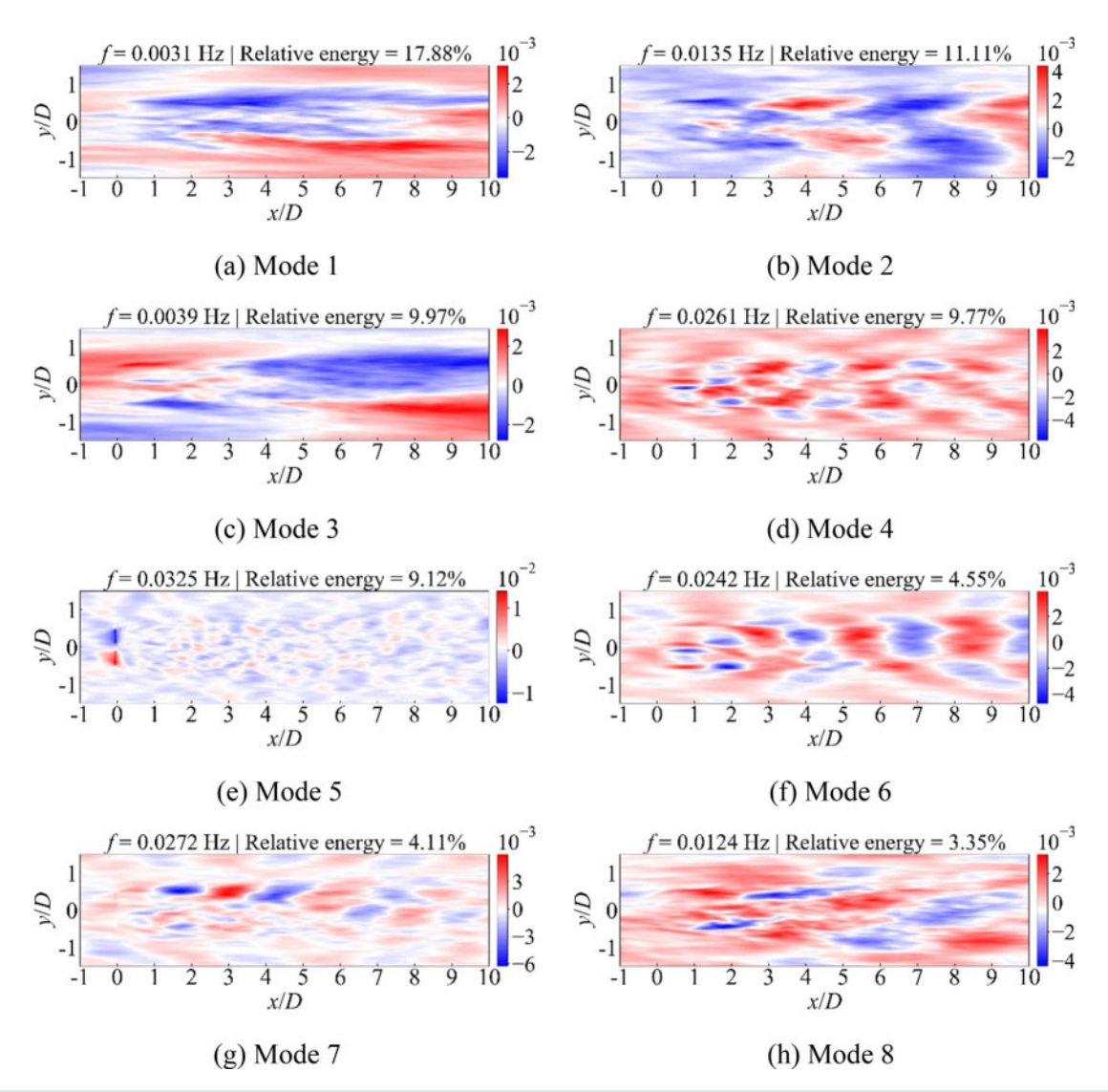


FIG. 22. The DMD modes of case 2 on the horizontal plane at hub height.

the base flow for DMD decomposition. This modification can influence the resulting frequencies and spatial features of the unsteady modes. In addition, the platform motion introduces extra perturbations into the flow, which may excite certain unsteady modes and increase their relative energy contributions. Despite the presence of new disturbance features induced by platform motion, several highenergy modes in the FOWT case still exhibit coherent structures similar to those found in the background turbulent flow. Moreover, the dominant mode frequencies in both FOWT and FBWT cases are significantly lower than the rotor rotation and platform motion frequencies. Although some modal spatial structures reflect the influence of the wind turbine, the fact that these dominant modes occur at low frequencies suggests that the wake dynamics are more strongly governed by the background turbulence. This suggests that the modulation effect of background turbulence on the wake of FOWTs remains significant.

To further analyze the modulation effect of platform motion on the wake, this study extracts DMD modes whose frequencies are close to the platform motion frequencies for each case, as shown in Fig. 24. It should be noted that DMD captures the actual response frequencies present in the flow field, which may deviate slightly from the prescribed platform motion frequencies due to background turbulence and other disturbances. Nonetheless, the spatial structures of these modes clearly indicate that they are motion-induced response modes. The results show that for all FOWT cases, one or two unsteady modes with frequencies close to the platform motion frequency are typically observed. These frequencies are generally higher than those of the dominant modes in the corresponding FBWT cases. The spatial structures of these modes reveal distinct coherent patterns in the wake disturbances induced by platform motion, significantly affecting the velocity distribution in the wake region. Due to differences in the total

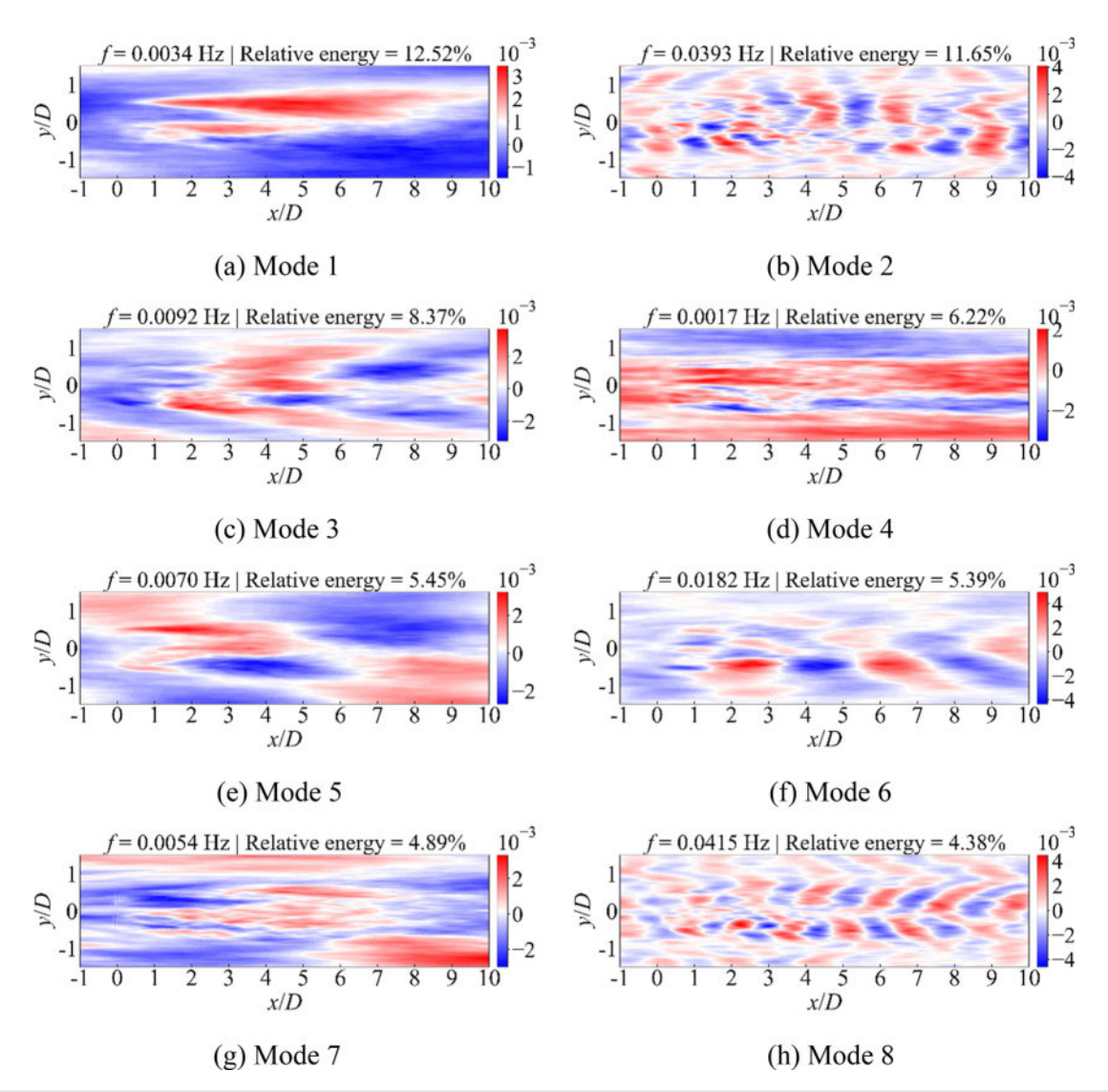


FIG. 23. The DMD modes of case 5 on the horizontal plane at hub height.

energy among cases, the mode indices may vary; however, a higher relative energy contributes more significantly to the unsteady evolution of the flow. It is also worth noting that some modes exhibit relatively low energy but present clear periodic structures in space, indicating that platform motion can excite physically meaningful coherent structures. A comparison across cases with different motion amplitudes and frequencies reveals that the amplitude primarily influences the strength of the disturbances-higher amplitudes lead to higher modal energy. In contrast, the frequency has a stronger impact on the spatial extent of the disturbance. For instance, when the motion frequency is 0.05 Hz, the coherent structures extend downstream up to approximately 4D. However, when the frequency increases to 0.2 Hz, the influence is confined within 2D. This may be due to two reasons: (1) the background turbulence predominantly contains low-frequency components, and under such low-frequency motion, the energy of

large-scale structures dissipates more slowly and can propagate farther downstream and (2) lower-frequency motions are closer to the natural response frequency of the wind turbine system, resulting in a resonance-like effect that enhances the periodic response in the wake. This enhanced periodicity may also contribute to increased wake meandering, leading to a broader wake, greater Gaussian standard deviation, and more pronounced centerline deflection, which, in turn, may delay wake recovery. Moreover, comparing the response modes under different turbulence intensities shows that at a turbulence intensity of 2.82%, the relative energy of motion-induced modes increases significantly. In some cases, two modes with similar frequencies can be identified, and the spatial extent of the disturbances becomes larger. This indicates that in low-turbulence environments, the modulation effect of platform motion on the wake is more pronounced. In contrast, at high turbulence intensity, the background

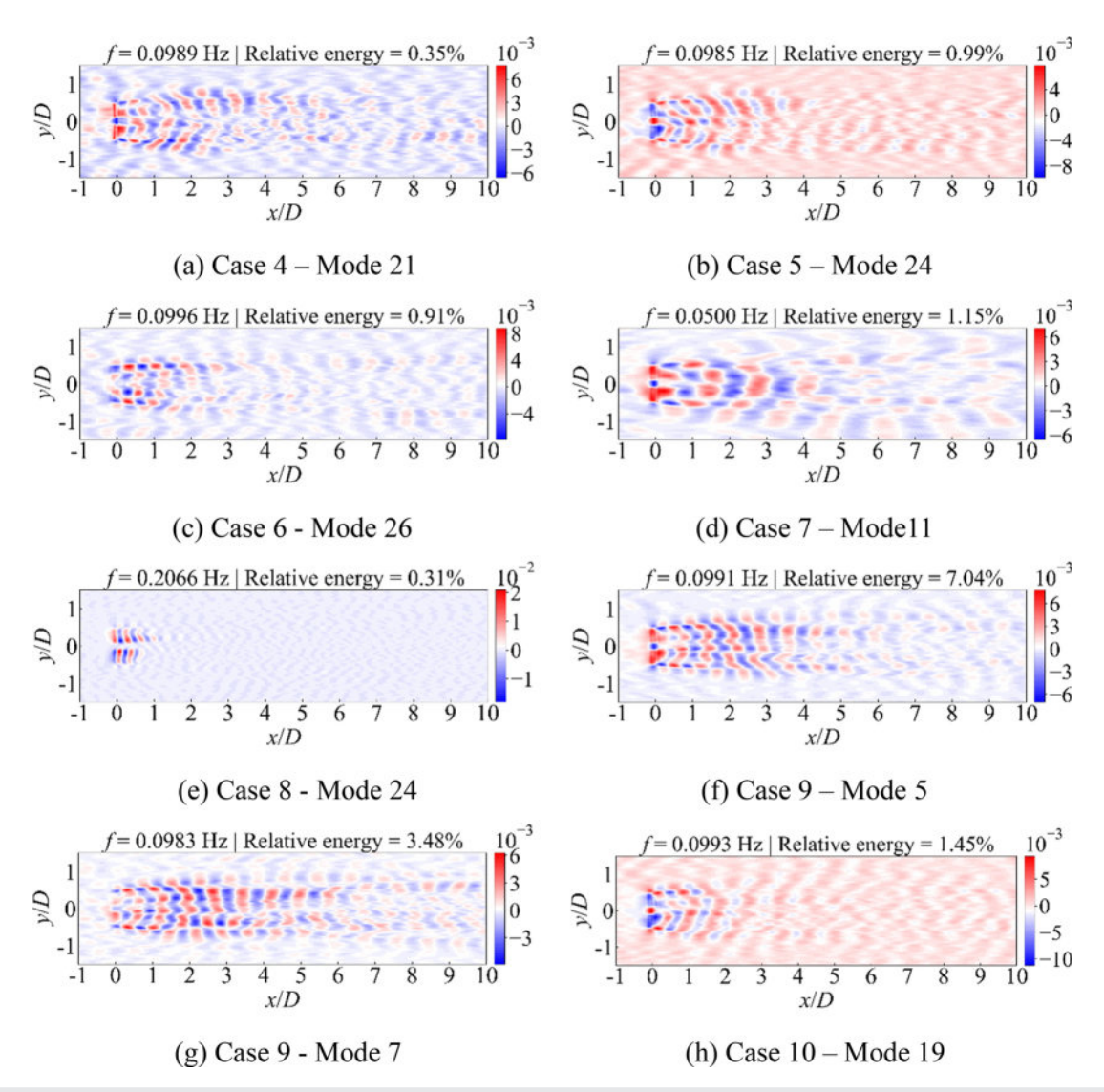


FIG. 24. The DMD modes corresponding to platform motion frequencies for all FOWT cases on the horizontal plane at the hub height.

turbulence dominates the unsteady evolution of the wake, thereby suppressing the disturbance effects induced by platform motion. These findings, from the perspective of modal energy and structural characteristics, further confirm that the differences in wake structures between FOWTs and FBWTs are more pronounced under low-turbulence or uniform inflow conditions.

Figure 25 presents the DMD modes corresponding to the platform motion frequencies for all FOWT cases on the vertical plane through the rotor center. The results show that, on the vertical plane, one or two unsteady modes with frequencies close to the platform motion frequencies can also be identified for the FOWT cases. Although the overall patterns are consistent with those observed on the horizontal plane, several notable differences are observed. Specifically, in the case with an inflow turbulence intensity of 2.82%, although the relative energy of the motion-induced mode is slightly higher than that in high-turbulence cases, the increase is not significant. This may be attributed to the directional characteristics of turbulence in this case, where the vertical disturbances are relatively stronger, which may more effectively suppress the periodic responses induced by platform motion. Among all cases, case 7 exhibits the most prominent modal energy contribution (17.4%), significantly higher than in other cases. In addition to the aforementioned factors, this may also be attributed to the fact that the pitch motion primarily acts in the vertical direction, which may have excited stronger unsteady vertical responses in this case. The marked rise in modal energy in case 7 may also be attributed to the fact that its motion frequency overlaps the characteristic frequency band of shear layer instability associated with wake meandering. <sup>14</sup> This overlap enhances the amplitude of wake meandering and strengthens the motion-induced contribution to the modal energy. To further verify this interpretation, a

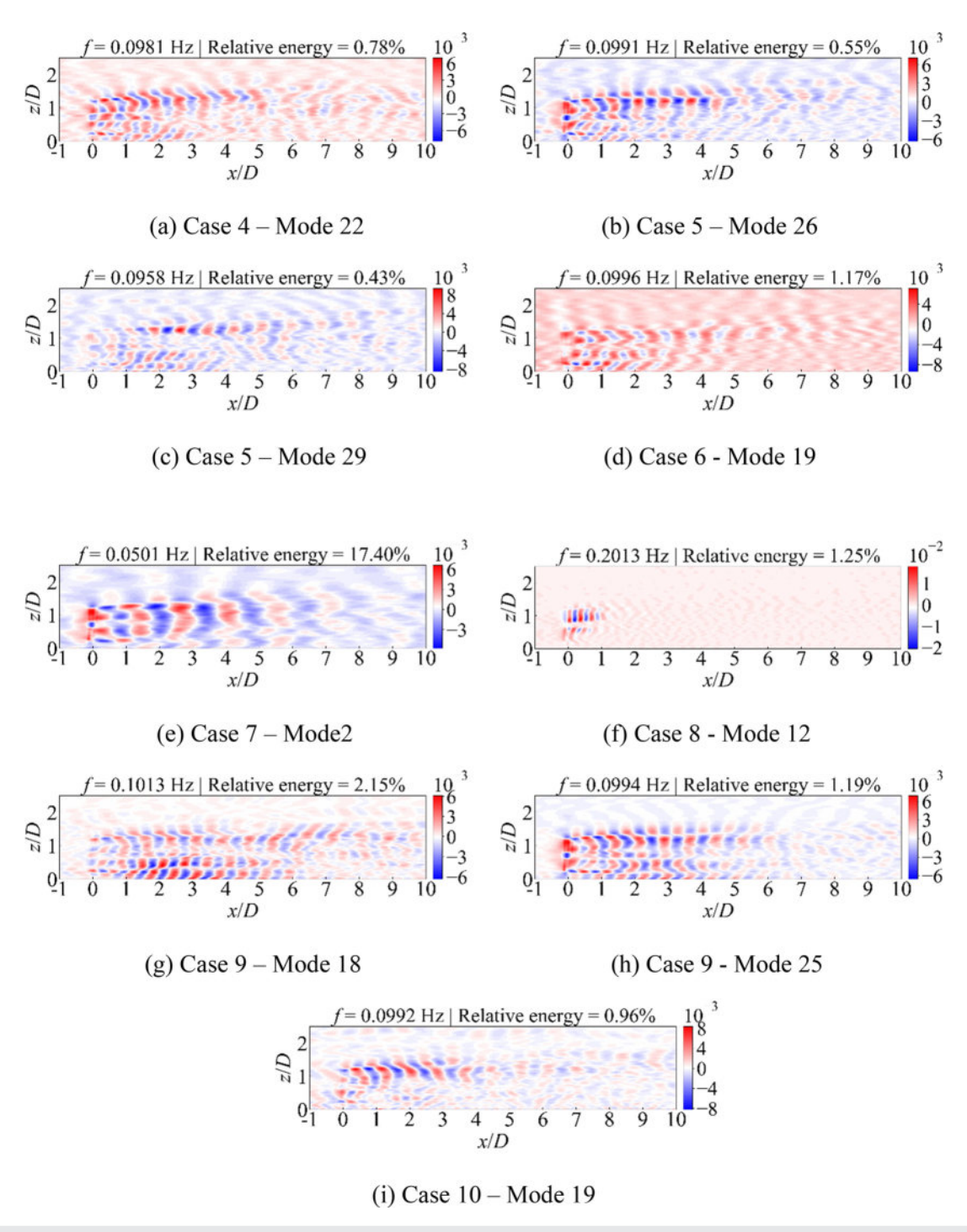
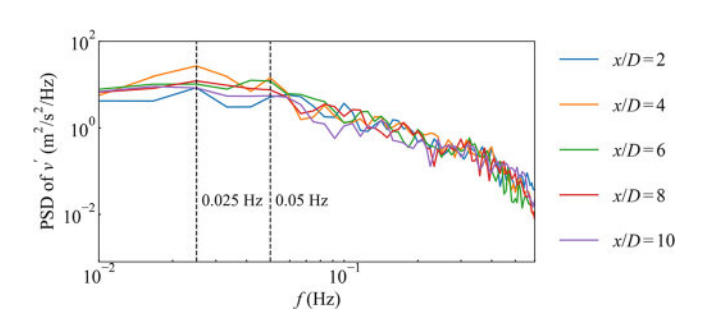


FIG. 25. The DMD modes corresponding to platform motion frequencies for all FOWT cases on the vertical plane through the rotor center.

power spectral density (PSD) analysis is performed using the spanwise velocity fluctuations at five sampling points along the streamwise centerline at hub height (x/D = 2, 4, 6, 8,and 10), as shown in Fig. 26. The dominant frequency consistently appears around 0.025 Hz, which

is approximately half of the platform motion frequency (0.05 Hz). This indicates a low-frequency synchronization between the platform motion and the wake meandering, suggesting that part of the motion energy is transferred into the wake through a resonance-like



**FIG. 26.** PSD of spanwise velocity fluctuations along the streamwise centerline at the hub height for case 7.

mechanism. The spatial structures further support this view, showing a stronger influence in the upper wake, especially near the shear layer adjacent to the freestream, where periodic disturbance patterns are evident. In contrast, the lower part of the wake exhibits weaker responses. This phenomenon is consistent with previous observations in the velocity field and vorticity structure analysis. In summary, from the perspective of DMD analysis, the dominant modes in the FOWT wake under ABL conditions primarily reflect the coherent structures of the background turbulence, and their evolution is significantly influenced by the inflow turbulence. Although variations in the amplitude and frequency of platform motion can excite distinct response modes, the motion-induced modes generally exhibit low energy contributions relative to the overall unsteady modes, indicating that their influence on the wake development remains limited.

## V. CONCLUSION

This study provides three main contributions: (i) investigating the wake evolution of FOWTs under realistic ABL inflow conditions; (ii) analyzing the effects of coupled surge–pitch motions on wake characteristics; and (iii) applying the DMD approach to identify dominant unsteady modes in wake dynamics. To achieve these objectives, LES coupled with the ALM to investigate the wake characteristics of FBWTs and FOWTs under ABL inflow conditions, focusing on the effects of combined surge–pitch platform motion. A comparative analysis is conducted to examine the influence of platform motion amplitude and frequency on wake characteristics under different inflow turbulence intensities. The main conclusions are as follows:

- The coupled surge-pitch motion primarily affects the aerodynamic performance of the FOWT by intensifying the fluctuations in instantaneous power and thrust. The fluctuation frequency matches the platform motion frequency, and larger motion amplitudes and frequencies lead to greater oscillation magnitudes. However, the influence on time-averaged power and thrust remains limited.
- 2. Compared to FBWTs, FOWTs exhibit faster wake recovery under ABL conditions. The disk-averaged streamwise velocity downstream of 3D can increase by up to 18.32%, with larger motion amplitudes and frequencies contributing more significantly to this enhancement. From the velocity deficit profiles, the influence of platform motion on wake recovery is most evident within the first 6D downstream under ABL conditions, beyond which the effect gradually diminishes. Gaussian fitting results show that FOWTs with stronger motions exhibit smaller standard deviations and larger centerline

displacements. While the horizontal wake centerline shifts farther from the center, the vertical wake centerline tends to remain closer to hub height. These results imply that the potential benefits of motion-induced wake recovery are confined to short downstream distances, and may be further shortened under higher inflow turbulence. In wind farm applications, this suggests that the spacing between the first-row and second-row turbines could be slightly reduced. However, when downstream turbines are simultaneously affected by the wakes of multiple FOWTs, the recovery characteristics become more complex and require further investigation before quantitative layout guidance can be established.

- 3. Instantaneous and phase-averaged vorticity field analysis reveals that platform motion induces periodic vortex structures in the near-wake, especially along the shear layer. These periodic features are generally observable within the first 4D downstream, where their spatial patterns remain relatively clear. Further downstream, the coherence of these structures weakens, especially under higher turbulence conditions.
- 4. Using DMD analysis, this study identifies and compares the unsteady modal characteristics of FBWT and FOWT wakes. From the perspective of modal frequency and spatial structure, the dominant modes are primarily influenced by the background ABL turbulence, indicating that inflow turbulence plays a major role in shaping unsteady wake dynamics. In FOWT cases, platform motion excites response modes with frequencies close to the motion frequency. These modes exhibit distinct spatial features associated with the platform motion; however, their energy contribution is generally lower compared to the total unsteady modal energy-typically below 2% in most cases. The lowerfrequency motions tend to excite higher-energy modes and induce more pronounced wake responses. For instance, when the motion frequency is 0.05 Hz, the energy contribution of motioninduced mode on the vertical plane can reach up to 17.4%. Moreover, DMD analysis on the vertical plane through the rotor center reveals that platform motion has a stronger impact on the upper part of the wake, particularly in the shear layer region near the freestream.

The investigation of time-averaged and unsteady wake characteristics of FOWTs under surge-pitch coupled motion in ABL conditions provides important insight that can support the development of analytical wake models, reduced-order modeling techniques, and other wake-related applications. In future work, further investigation will focus on the influence of other motion degrees of freedom and combined motions on wake development, along with the interactions among multiple FOWTs.

## **ACKNOWLEDGMENTS**

This work was supported by the National Natural Science Foundation of China (No. 52131102) and the National Key Research and Development Program of China (No. 2022YFC2806705), to which the authors are most grateful.

# AUTHOR DECLARATIONS Conflict of Interest

The authors have no conflicts to disclose.

### **Author Contributions**

Mingqiu Liu: Data curation (equal); Formal analysis (equal); Investigation (equal); Methodology (equal); Validation (equal); Visualization (equal); Writing – original draft (equal). Yao Zhong: Conceptualization (equal); Project administration (equal); Resources (equal). Weiwen Zhao: Conceptualization (equal); Funding acquisition (equal); Methodology (equal); Project administration (equal); Resources (equal); Software (equal); Supervision (equal); Writing – review & editing (equal). Decheng Wan: Conceptualization (equal); Funding acquisition (equal); Resources (equal); Supervision (equal).

### **DATA AVAILABILITY**

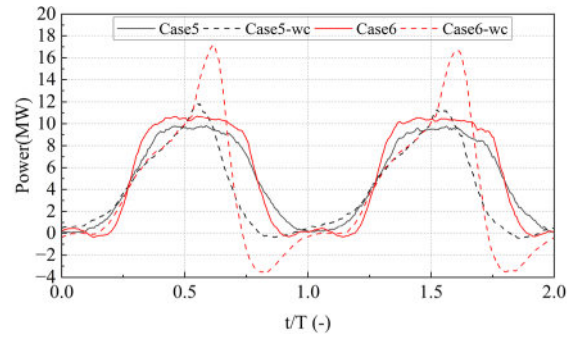
The data that support the findings of this study are available from the corresponding author upon reasonable request.

## APPENDIX A: CONTROL SENSITIVITY ANALYSIS

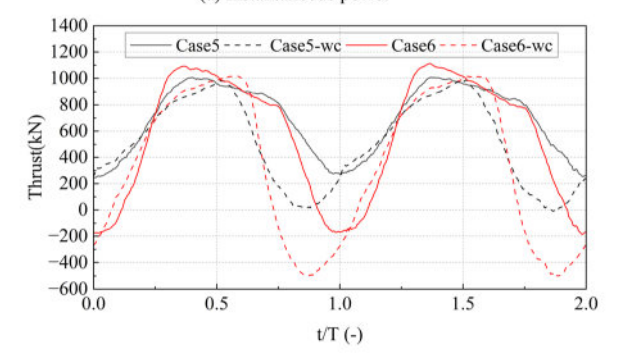
In order to assess the influence of the control system, additional simulations are conducted for cases 5 and 6 with a basic controller implemented. The wind turbine adopts a conventional variable-speed and collective-pitch control strategy, in which the generator torque regulates the rotor speed below rated wind speed and the pitch control maintains rated power above rated conditions. 30,31 Figure 27 presents the thrust and power of the wind turbine with and without control, where "wc" denotes the controlled cases. The results show that, once the controller is enabled, the fluctuations in rotor thrust and power become more pronounced, while the mean values are reduced. This behavior arises from the distinction between aerodynamic power extracted by the rotor and electrical power delivered by the generator. When the rotor power exceeds the rated generator output, the controller increases the blade pitch angle to shed the excess energy, leading to higher peaks in instantaneous rotor thrust and power. These trends are consistent with the findings reported by Yang et al. 32 and further indicate that applying a simple controller alone cannot prevent the occurrence of propeller states under large-amplitude platform motions.

Figure 28 shows the normalized velocity deficit profiles on the horizontal and vertical planes for cases with and without control. The results indicate that the wake velocity deficit becomes smaller when the controller is active. This is because, when the rotor power exceeds the generator capacity, the blade pitch angle increases to reduce power extraction, while at low rotor speed the minimum pitch is limited to 0° rather than negative values that would otherwise enhance power capture. Consequently, less energy is extracted from the flow during platform motion, resulting in a reduced wake deficit.<sup>32</sup> The control system modifies both the aerodynamic performance and the wake recovery of the FOWT. Nevertheless, the overall trend of velocity deficit recovery remains consistent with and without control. Therefore, the uncontrolled cases are still valuable for isolating the fundamental influence of platform motions on wake behavior and provide a useful reference when evaluating the additional effects of advanced control strategies.

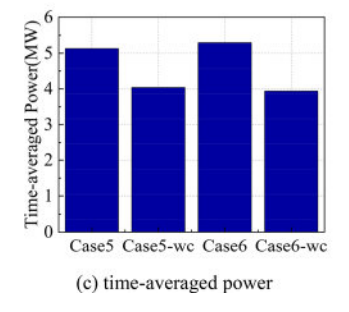
Figure 29 shows the minimum thrust values obtained under the same settings as case 5, where the ratios between surge  $(A_s)$  and



(a) instantaneous power







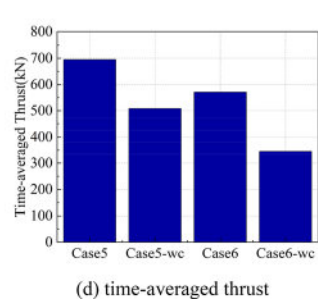


FIG. 27. The thrust and power of the wind turbine with and without control.

pitch  $(A_p)$  motion amplitudes are kept equal and the motion frequency is fixed at 0.1 Hz. Note that the surge amplitude is given in meters and the pitch amplitude in degrees, but their numerical values are set equal. The results indicate that the threshold amplitude at which negative thrust occurs is about 6.27, estimated by linear interpolation between the cases with amplitudes of 6.2 and 6.3. It should be noted that the occurrence of the propeller state is influenced by multiple factors, such as inflow wind speed, motion amplitude, and frequency, and the present study reports the threshold only for this specific operating condition.

## APPENDIX B: GAUSSIAN FITTING ACCURACY

Figure 30 shows the coefficients of determination  $(R^2)$  of the Gaussian fits in the horizontal and vertical directions. Gaussian fitting is performed every 6 m downstream. The  $R^2$  values range from 0.96 to 0.99 within 4–5D and increase further downstream,

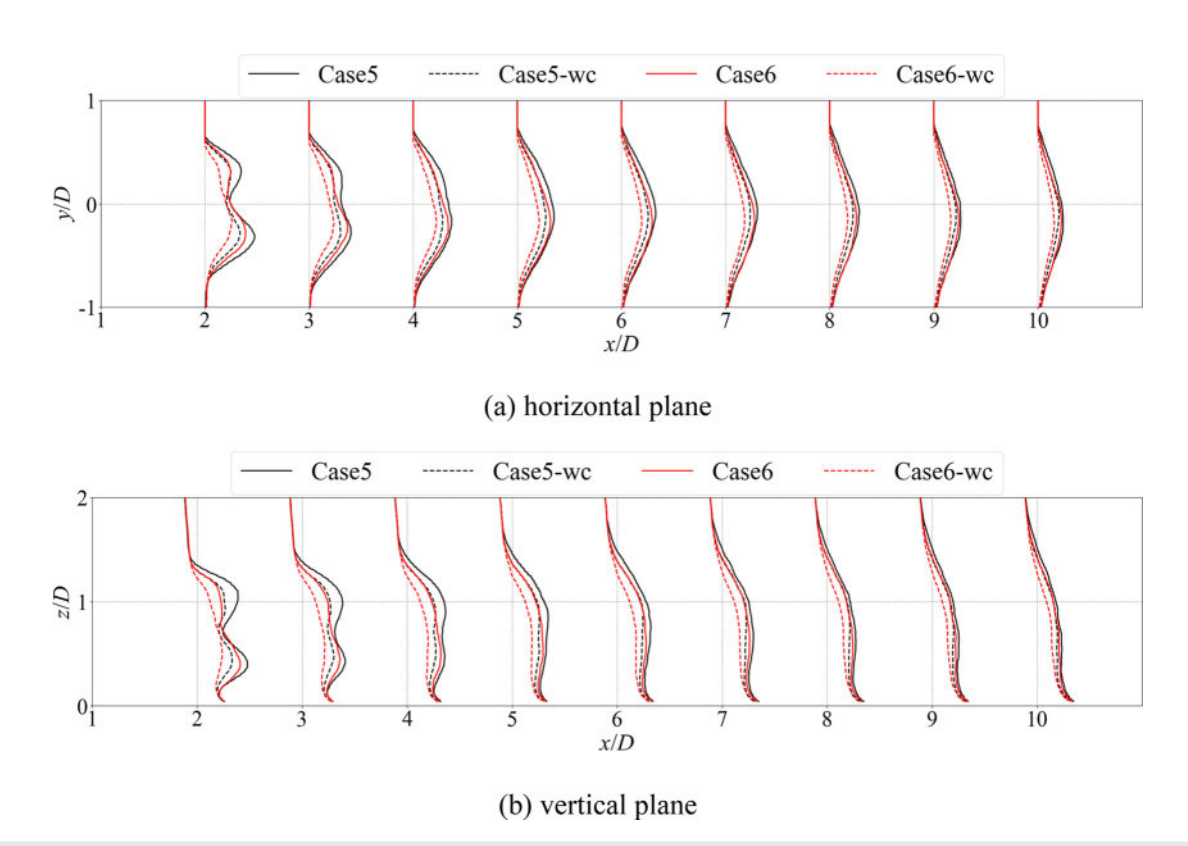


FIG. 28. The normalized velocity deficit profiles on the horizontal and vertical planes.

remaining around 0.99 beyond 5D, indicating generally high fitting accuracy.

Figure 31 shows the normalized velocity deficit profiles from LES with the corresponding Gaussian fits for case 5 on the horizontal and vertical planes. At the downstream location of 4D, the velocity deficit has not yet developed into a self-similar Gaussian shape and, therefore, the fitting shows slightly lower accuracy. Nevertheless, the Gaussian function captures the main features of the velocity deficit further downstream and agrees well with the LES results. Figure 32 shows the 95% confidence intervals of the fitted parameters for case 5, where the shaded regions indicate the confidence ranges. These intervals quantify the statistical uncertainty of the fitted parameters. Overall, the Gaussian fitting used in this study provides an accurate and robust representation of the velocity deficit profiles.

# APPENDIX C: DMD RECONSTRUCTION ACCURACY

Figure 33 shows the relationship between the sampling interval and the reconstruction error. The results indicate that the error gradually increases with a larger sampling interval, mainly because fewer snapshots are available to capture the temporal dynamics and the resolvable frequency band becomes narrower. In the present study, a sampling interval of 0.2 s is adopted. Figure 34 presents the reconstruction errors on both the horizontal and vertical planes for different cases. The errors remain at relatively low

levels across all cases, demonstrating the overall accuracy of the DMD decomposition.

Figures 35 and 36 compare the LES and DMD-reconstructed results at the final time step for case 5 on the horizontal and vertical planes, respectively. Although some errors exist in the reconstructed

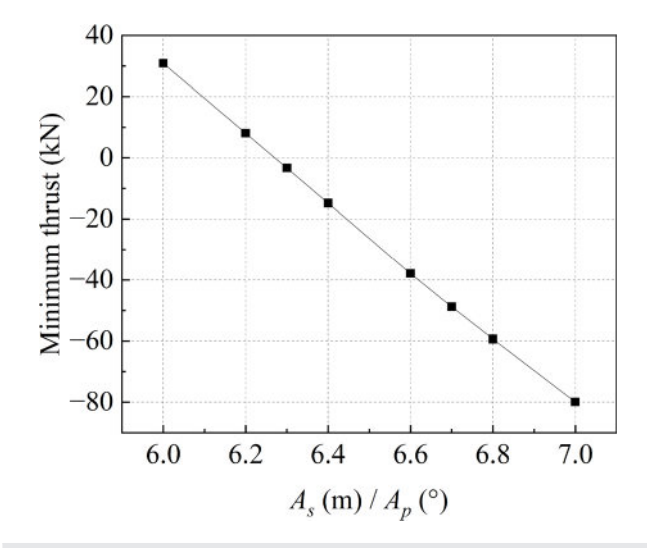


FIG. 29. The minimum thrust under different motion amplitudes.

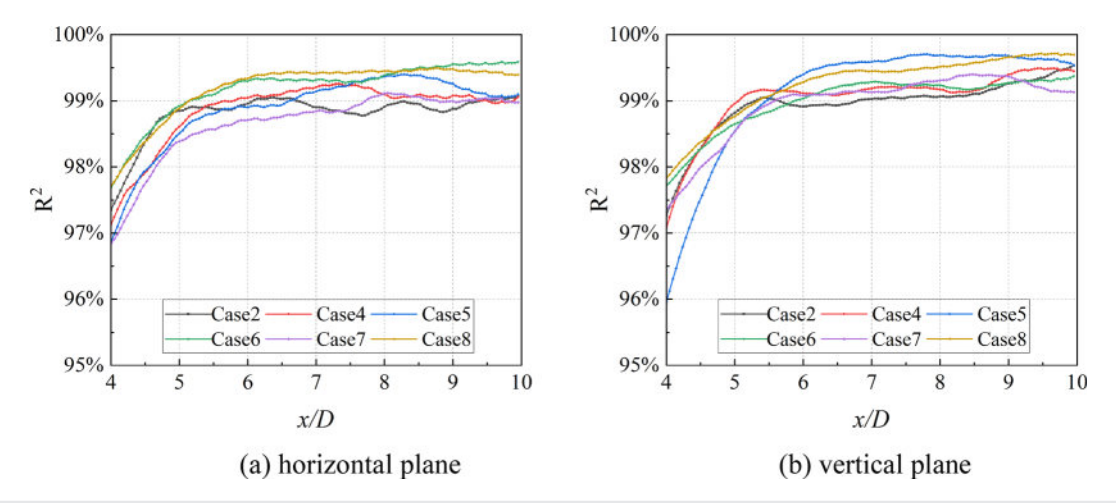


FIG. 30. The R<sup>2</sup> of the Gaussian fits in the horizontal and vertical directions.

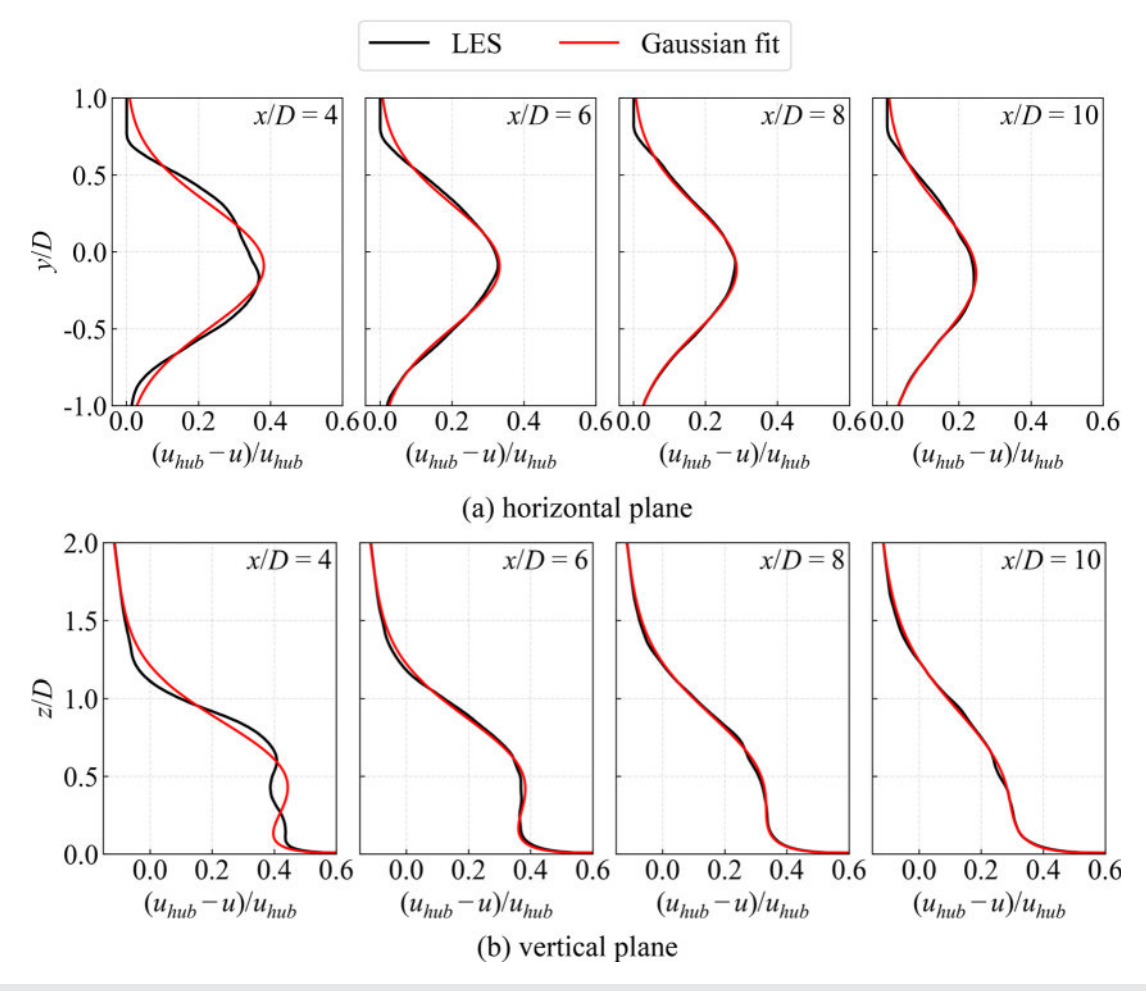


FIG. 31. The normalized velocity deficit profiles from the LES and Gaussian fits for case 5.

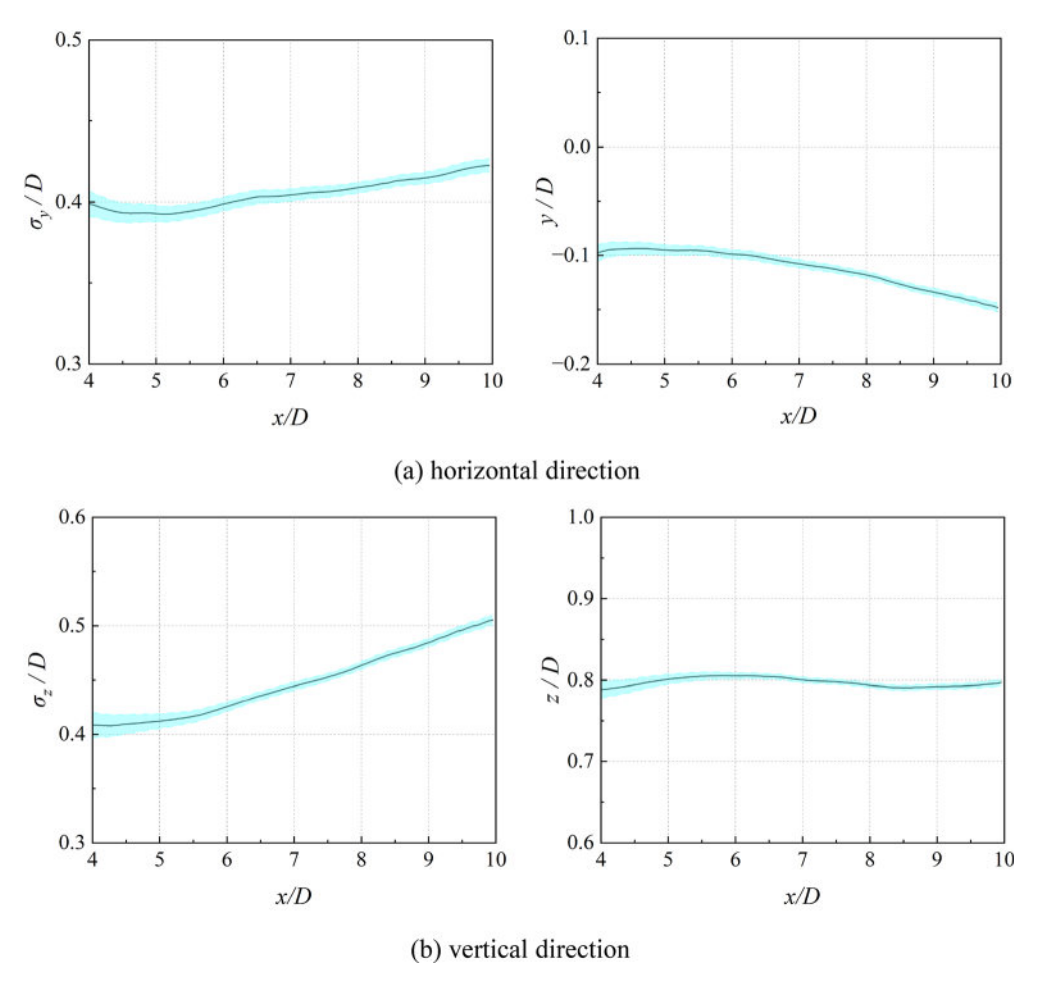
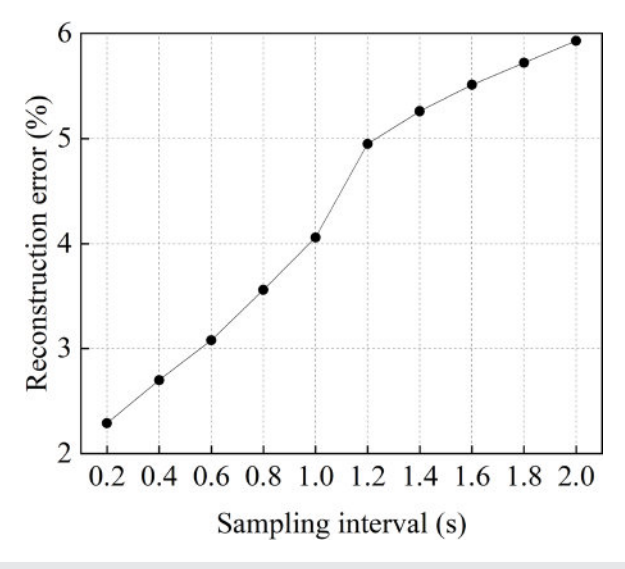


FIG. 32. The Gaussian fitting results with 95% confidence intervals for case 5.



**FIG. 33.** Variation of reconstruction error with sampling interval.

wake velocity, the main flow features are well reconstructed. In particular, the shear layer, the periodic coherent structures, and the wake meandering are clearly captured. This confirms that the DMD analysis is capable of capturing the dominant unsteady wake dynamics.

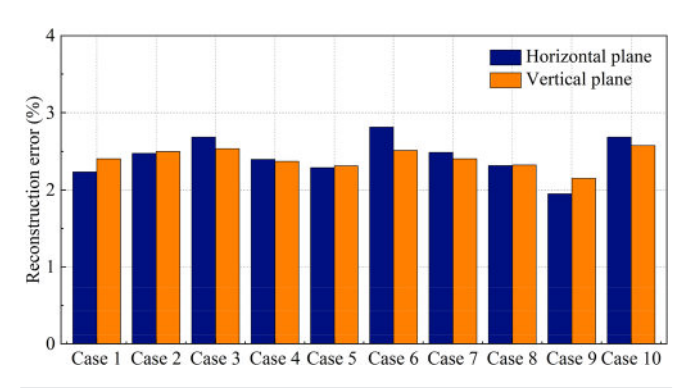


FIG. 34. Reconstruction errors on the horizontal and vertical planes for cases.

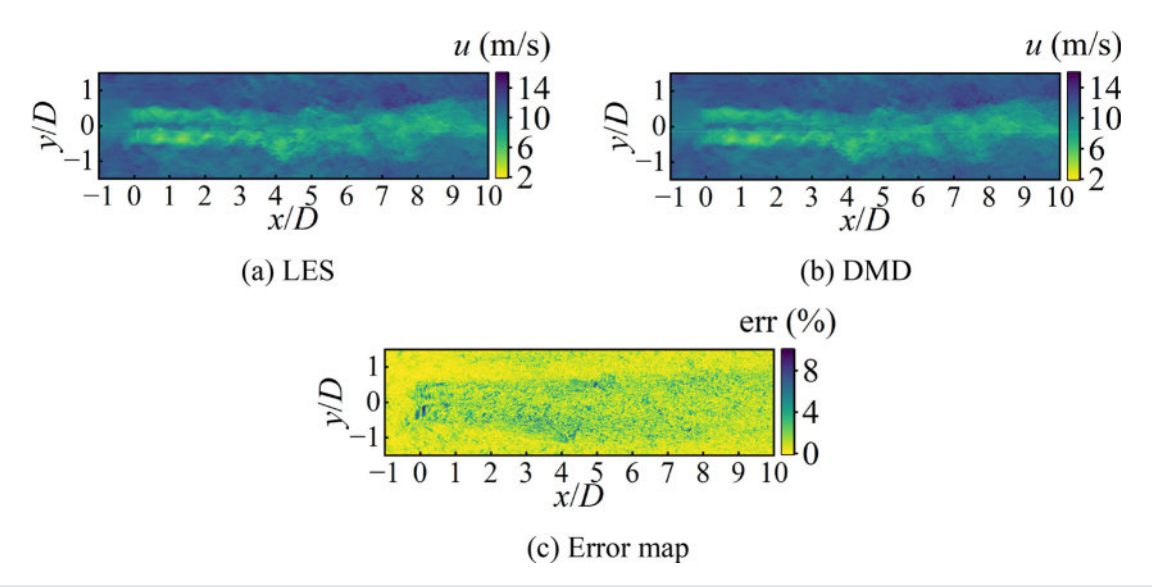


FIG. 35. Comparison between LES and DMD-reconstructed velocity fields on the horizontal plane at the final time step for case 5.

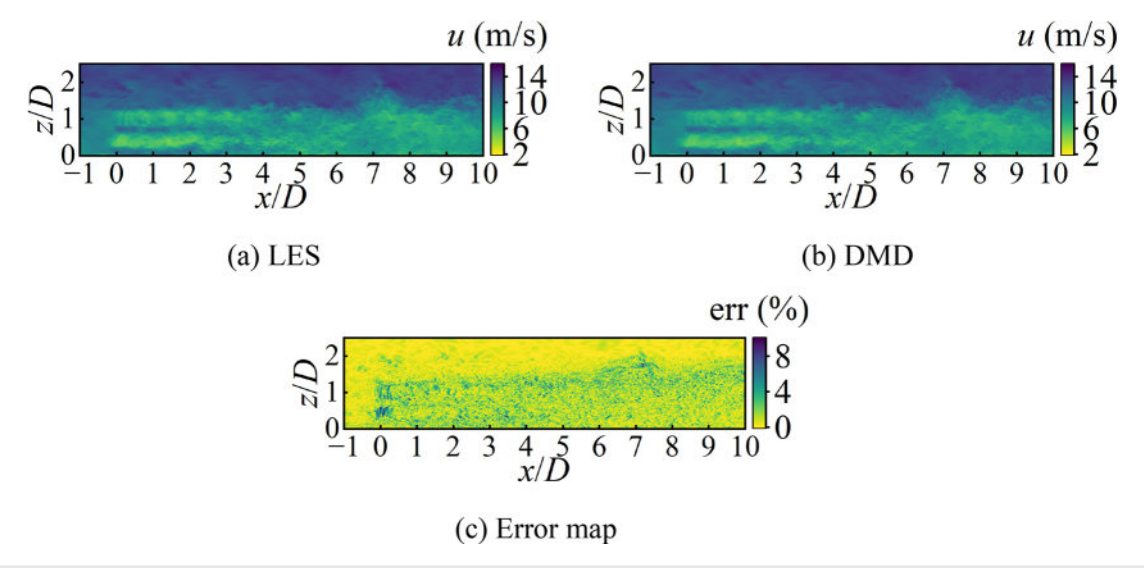


FIG. 36. Comparison between LES and DMD-reconstructed velocity fields on the vertical plane at the final time step for case 5.

## **REFERENCES**

Bhattacharya and G. Nikitas, "Wind energy: Status and outlook with focus on offshore wind," in *Energy and Climate Change* (Elsevier, 2025), pp. 197–224.
 L. Wang, M. Dong, J. Yang, L. Wang, S. Chen, N. Duić, Y. H. Joo, and D. Song, "Wind turbine wakes modeling and applications: Past, present, and future," Ocean Eng. 309, 118508 (2024).

<sup>3</sup>Y.-X. Qiu, X.-D. Wang, S. Kang, M. Zhao, and J.-Y. Liang, "Predictions of unsteady HAWT aerodynamics in yawing and pitching using the free vortex method," Renewable Energy **70**, 93–106 (2014).

<sup>4</sup>B. Wen, X. Tian, X. Dong, Z. Peng, and W. Zhang, "Influences of surge motion on the power and thrust characteristics of an offshore floating wind turbine," Energy 141, 2054–2068 (2017).

<sup>5</sup>H. Lee and D.-J. Lee, "Effects of platform motions on aerodynamic performance and unsteady wake evolution of a floating offshore wind turbine," Renewable Energy 143, 9–23 (2019).

<sup>6</sup>T. T. Tran and D.-H. Kim, "A CFD study into the influence of unsteady aerodynamic interference on wind turbine surge motion," Renewable Energy **90**, 204–228 (2016).

<sup>7</sup>Y. Fang, L. Duan, Z. Han, Y. Zhao, and H. Yang, "Numerical analysis of aero-dynamic performance of a floating offshore wind turbine under pitch motion," Energy 192, 116621 (2020).

<sup>8</sup>Y. Fang, G. Li, L. Duan, Z. Han, and Y. Zhao, "Effect of surge motion on rotor aerodynamics and wake characteristics of a floating horizontal-axis wind turbine," Energy 218, 119519 (2021).

<sup>9</sup>Z. Chen, X. Wang, Y. Guo, and S. Kang, "Numerical analysis of unsteady aerodynamic performance of floating offshore wind turbine under platform surge and pitch motions," Renewable Energy 163, 1849–1870 (2021).

<sup>10</sup>G. Chen, X.-F. Liang, and X.-B. Li, "Modelling of wake dynamics and instabilities of a floating horizontal-axis wind turbine under surge motion," Energy 239, 122110 (2022).

- <sup>11</sup>Y. Guo, X. Wang, Y. Mei, Z. Ye, and X. Guo, "Effect of coupled platform pitch-surge motions on the aerodynamic characters of a horizontal floating offshore wind turbine," Renewable Energy 196, 278–297 (2022).
- <sup>12</sup>Y. Cai, X. Li, S. Leng, H. Zhao, and Y. Zhou, "Effect of combined surge and pitch motion on the aerodynamic performance of floating offshore wind turbine," Ocean Eng. 306, 118061 (2024).
- <sup>13</sup>K. Wang, M. Zhao, Q. Tang, and R. Zha, "Investigating effects of pitch motions on aerodynamics and wake characteristics of a floating offshore wind turbine," <u>Energy Convers. Manage.</u> 326, 119402 (2025).
- <sup>14</sup>Z. Li, G. Dong, and X. Yang, "Onset of wake meandering for a floating offshore wind turbine under side-to-side motion," J. Fluid Mech. 934, A29 (2022).
- <sup>15</sup>A. Arabgolarcheh, D. Micallef, A. Rezaeiha, and E. Benini, "Modelling of two tandem floating offshore wind turbines using an actuator line model," Renewable Energy 216, 119067 (2023).
- <sup>16</sup>A. Arabgolarcheh, D. Micallef, and E. Benini, "The impact of platform motion phase differences on the power and load performance of tandem floating offshore wind turbines," Energy 284, 129271 (2023).
- <sup>17</sup>L. Yang, "Investigation of wake characteristics of floating offshore wind turbine with control strategy using actuator curve embedding method," Renewable Energy 218, 119255 (2023).
- <sup>18</sup>Y. Li, W. Yu, and H. Sarlak, "Wake structures and performance of wind turbine rotor with harmonic surging motions under laminar and turbulent inflows," Wind Energy 27(12), 1499–1525 (2024).
- <sup>19</sup>J. Yang, Z. Liu, W. Hu, S. Liu, and N. Wang, "A study on the wake model of floating wind turbine with swaying motions based on an improved actuator disk method," Phys. Fluids 36, 085114 (2024).
- 20 T. Zhou, H. Lan, C. Xu, X. Han, and X. Wu, "Wake and performance of floating offshore wind turbines under six degrees of freedom conditions," Phys. Fluids 37(1), 015167 (2025).
- <sup>21</sup>Z. Yu, Q. Ma, X. Zheng, K. Liao, H. Sun, and A. Khayyer, "A hybrid numerical model for simulating aero-elastic-hydro-mooring-wake dynamic responses of floating offshore wind turbine," Ocean Eng. 268, 113050 (2023).
- <sup>22</sup>Y. Huang, W. Zhao, and D. Wan, "Wake interaction between two spar-type floating offshore wind turbines under different layouts," Phys. Fluids 35(9), 097102 (2023).
- <sup>23</sup>S. Xu, X. Yang, W. Zhao, and D. Wan, "Numerical analysis of aero-hydrodynamic wake flows of a floating offshore wind turbine subjected to atmospheric turbulence inflows," Ocean Eng. 300, 117498 (2024).
- <sup>24</sup>G. De Cillis, S. Cherubini, O. Semeraro, S. Leonardi, and P. De Palma, "The influence of incoming turbulence on the dynamic modes of an NREL-5MW wind turbine wake," Renewable Energy 183, 601–616 (2022).
- 25 T. Wang, C. Cai, J. Liu, C. Peng, Y. Wang, X. Sun, X. Zhong, J. Zhang, and Q. Li, "Wake characteristics and vortex structure evolution of floating offshore wind turbine under surge motion," Energy 302, 131788 (2024).
- <sup>26</sup>F. Manganelli, C. Bernardi, A. Giannotta, S. Leonardi, S. Cherubini, and P. De Palma, "The effect of Coriolis force on the coherent structures in the wake of a 5MW wind turbine," Energy Convers. Manage.: X 25, 100830 (2025).
- <sup>27</sup>X. Zhang, M. Tao, M. Zhang, R. Zhu, S. Wang, B. Li, B. Liu, and Z. Xie, "Aerodynamic and wake characteristics for full-scale and model-scale 5 MW wind turbines using data-driven modal decomposition," Ocean Eng. 318, 120131 (2025).
- <sup>28</sup>J. Smagorinsky, "General circulation experiments with the primitive equations:

   I. The basic experiment\*," Mon. Weather Rev. 91(3), 99–164 (1963).

- <sup>29</sup>M. J. Churchfield, S. Lee, J. Michalakes, and P. J. Moriarty, "A numerical study of the effects of atmospheric and wake turbulence on wind turbine dynamics," J. Turbul. 13, N14 (2012).
- 30]. N. Sørensen and W. Z. Shen, "Numerical modeling of wind turbine wakes," J. Fluids Eng. 124(2), 393–399 (2002).
- <sup>31</sup>J. Jonkman, S. Butterfield, W. Musial, and G. Scott, "Definition of a 5-MW reference wind turbine for offshore system development," Report No. NREL/TP-500-38060, 947422 (National Renewable Energy Laboratory, 2009).
- <sup>32</sup>L. Yang, K. Liao, Q. Ma, A. Khayyer, and H. Sun, "Coupled aero-servo-elastic method for floating offshore wind turbine wake analysis," Ocean Eng. 307, 118108 (2024).
- 33S. Liu, Z. Xin, L. Wang, Z. Cai, and E. Benini, "Numerical study on the impact of structural flexibility and platform motions on the dynamic behaviors and wake characteristics of floating offshore wind turbine," Phys. Fluids 37(6), 067153 (2025)
- <sup>34</sup>Z. Li, Y. Zhang, X. Zhang, D. Li, Z. He, and Q. Wang, "Effect of nacelle and tower on wind turbine wake," in 3rd International Conference on Advanced Electrical and Energy Systems (AEES) (IEEE, Lanzhou, China, 2022), pp. 52–56.
- 35S. Liu, Z. Xin, L. Wang, and Z. Cai, "Fluid-structure interaction simulation of dynamic response and wake of floating offshore wind turbine considering tower shadow effect," Acta Mech. Sin. 40(8), 323567 (2024).
- <sup>36</sup>C.-H. Moeng, "A large-eddy-simulation model for the study of planetary boundary-layer turbulence," J. Atmos. Sci. 41(13), 2052–2062 (1984).
- <sup>37</sup>K. S. Hansen, R. J. Barthelmie, L. E. Jensen, and A. Sommer, "The impact of turbulence intensity and atmospheric stability on power deficits due to wind turbine wakes at Horns Rev wind farm," Wind Energy 15(1), 183–196 (2012).
- <sup>38</sup>G. M. Stewart, A. Robertson, J. Jonkman, and M. A. Lackner, "The creation of a comprehensive metocean data set for offshore wind turbine simulations," Wind Energy 19(6), 1151–1159 (2016).
- 39 M. Philippe, A. Babarit, and P. Ferrant, "Modes of response of an offshore wind turbine with directional wind and waves," Renewable Energy 49, 151–155 (2013).
- <sup>40</sup>P. Doubrawa, M. J. Churchfield, M. Godvik, and S. Sirnivas, "Load response of a floating wind turbine to turbulent atmospheric flow," Appl. Energy 242, 1588–1599 (2019).
- <sup>41</sup>T. Li, Y. Zhang, Q. Yang, X. Zhou, Z. Zhang, and T. Wang, "Unsteady aerodynamic characteristics of a floating offshore wind turbine in propeller state," Renewable Energy 246, 122861 (2025).
- <sup>42</sup>A. Fu, Y. Liu, Z. Liu, H. Liu, X. Liu, C. Song, and Z. Zhang, "Gaussian process-enhanced predictive control for individual pitch regulation in floating offshore wind turbines," Ocean Eng. 332, 121394 (2025).
- <sup>43</sup>N. O. Jensen, "A note on wind generator interaction," Risø-M, Report No. 2411 (Risø National Laboratory, 1983).
- 44M. Bastankhah and F. Porté-Agel, "A new analytical model for wind-turbine wakes." Renewable Energy 70, 116-123 (2014).
- <sup>45</sup>Z. Zhang, P. Huang, and H. Sun, "A novel analytical wake model with a cosine-shaped velocity deficit," Energies 13(13), 3353 (2020).
- <sup>46</sup>R. He, H. Yang, H. Sun, and X. Gao, "A novel three-dimensional wake model based on anisotropic Gaussian distribution for wind turbine wakes," Appl. Energy 296, 117059 (2021).
- <sup>47</sup>T. Messmer, J. Peinke, A. Croce, and M. Hölling, "The role of motion-excited coherent structures in improved wake recovery of a floating wind turbine," J. Fluid Mech. 1018, A23 (2025).
- <sup>48</sup>P. J. Schmid, "Dynamic mode decomposition of numerical and experimental data," J. Fluid Mech. 656, 5–28 (2010).